Dopaminergic regulation of vestibulo-cerebellar circuits through unipolar brush cells

Jose Ernesto Canton-Josh, Joanna Qin, Joseph Salvo, Yevgenia Kozorovitskiy*

Department of Neurobiology, Northwestern University, Evanston, IL 60208

*Corresponding author: Yevgenia.Kozorovitskiy@northwestern.edu

SUMMARY

While multiple monoamines modulate cerebellar output, the mechanistic details of dopaminergic signaling in the cerebellum remain poorly understood. Here we show that Drd1 dopamine receptors are expressed in unipolar brush cells (UBCs) of the cerebellar vermis. Drd1 activation increases UBC firing rate and postsynaptic NMDA receptor-mediated currents. Using anatomical tracing and *in situ* hybridization, we tested three hypotheses about the source of cerebellar dopamine. We exclude midbrain dopaminergic nuclei and tyrosine hydroxylase-positive Purkinje cells as potential sources, supporting the possibility of dopaminergic co-release from locus coeruleus (LC) axons. Using an optical dopamine sensor $GRAB_{DA}$, electrical stimulation, and optogenetic activation of LC fibers in the acute slice, we find evidence for monoamine release onto Drd1-expressing UBCs. Altogether, we propose that the LC regulates cerebellar cortex activity by co-releasing dopamine onto UBCs to modulate their response to cerebellar inputs. Purkinje neurons directly inhibit these Drd1-positive UBCs, forming a dopamine-sensitive recurrent vestibulo-cerebellar circuit.

INTRODUCTION

Cerebellar activity plays a critical function in fine motor learning (Kalmbach et al., 2010; Raymond and Lisberger, 1998; Woodruff-pak, 1993). The cerebellum is defined by its clearly organized cytoarchitecture; however, important anatomical, molecular, and functional differences between lobules are beginning to emerge. These differences include specialized neuronal classes present only in certain regions of the cerebellar cortex. Electrophysiological and behavioral data indicate that these varying motifs are likely relevant for the function of specific lobules in behavior. One key difference between cerebellar lobules is the distribution of unipolar brush cells (UBCs), a glutamatergic interneuron enriched in the granular layer of vestibulo-cerebellum, which is known to be involved in processing vestibular sensory input (Mugnaini and Floris, 1994). UBCs reside in the granular layer and receive inputs from mossy fibers. Each UBC axon diverges, releasing glutamate onto multiple local granule cells or other UBCs. Since UBCs are recurrently connected, they are poised to amplify and temporally extend the influence of excitatory inputs into the cerebellum (Requarth and Sawtell, 2014). Alternatively, UBCs—receiving a single mossy fiber input—could form a 'labeled line' input to the granular layer, helping to distinguish between inputs from semicircular canals and vestibular nuclei (Balmer and Trussell, 2019). The relatively recent discovery of UBCs in the late 1970s (Altman and Bayer, 1977) and characterization in the 1990s (Mugnaini and Floris, 1994), their sparseness in the cerebellum, and the lack of tools to isolate them have limited our understanding of their functional connectivity.

Differences in inputs and expression patterns of neuromodulatory receptors also distinguish cerebellar regions (Cerminara et al., 2015). While it is clear that norepinephrine (NE) regulates cerebellar output, the mechanistic details of neuromodulatory effects for other amines remain poorly understood (Basile and Dunwiddie, 1984; Carey and Regehr, 2009; Lanore et al., 2019; Lippiello et al., 2015). Several previous reports posit the expression of dopamine type 1 receptor (Drd1a) within the granular layer of the cerebellum (Locke et al., 2018; Panagopoulos et al., 1993). Additionally, several groups have previously reported dopaminergic projections from the substantia nigra pars compacta (SNc) and the ventral tegmental area (VTA) targeting the cerebellar cortex of rats and monkeys (Melchitzky, 2000; Panagopoulos et al., 1991). Yet, recent work in mice did not find evidence for projections from midbrain dopaminergic nuclei to the cerebellum (Giovannucci et al., 2017). Another potential source of dopamine to the cerebellum is from a subset of tyrosine hydroxylase (TH) positive Purkinje (Pkj) cells. Vestibulo-cerebellar Pkj cells express tyrosine hydroxylase, the rate-limiting enzyme in the classical dopamine (DA) synthesis pathway (Abbott et al., 1996; Chung et al., 2009, 2010; Huang et al., 2016; Sawada et al., 2004; Takada et al., 1993). One prior report details dendritic release of DA by Pkj cells onto their own dendrites, expressing dopamine type 2 receptor (Drd2) (Kim et al., 2009). It is possible that these Pkj cells could also be the source of dopamine to local UBCs expressing Drd1 receptors. A third potential source of cerebellar DA is the locus coeruleus, recently demonstrated to release dopamine as well as norepinephrine in the hippocampus (Kawahara et al., 2001; Kempadoo et al., 2016; Takeuchi et al., 2016). The proposed

91 mechanism of action for this dual amine co-release is incomplete conversion of dopamine to
92 norepinephrine in the vesicles. If incomplete conversion also takes place in the cerebellum, then DA
93 release could enhance activity levels in the UBC network or coordinate the timing of their activity.

94 Altogether, previous research is consistent with the possibility of cerebellar DA signaling, but many
95 unknowns remain. Here, using a combination of anatomical characterization, electrophysiology, two-photon
96 laser scanning microscopy and glutamate photolysis, along with optogenetics and DA sensor imaging, we
97 resolve this uncertainty by characterizing the expression of Drd1a receptors in the cerebellar cortex,
98 defining the role of these receptors and the function of Drd1a-positive UBCs within cerebellar circuits, and
99 revealing the source of cerebellar DA.

100 **RESULTS**

101 **Expression of Drd1a receptors in UBCs of lobules IX/X**

102 Analysis of Drd1-EY262-Cre;tdTomato expression in the cerebellar cortex reveals numerous small
103 tdTomato+ (tdT) cells distributed across the cerebellar granular layer (**Figure 1A**), enriched in lobules IX
104 and X of the cerebellar vermis, lobules VIb and VII, and the paraflocculus. These regions of the cerebellum
105 are known to contain many UBCs. Confocal images confirm that cerebellar tdT+ cells possess the
106 morphological features of UBCs: a single large dendritic brush and a medium sized soma relative to
107 granule cells (**Figure 1B).** All tdT+ cells in the cerebellum were positive for nuclear protein Eomesodermin
108 (Tbr2), a known marker for all UBCs (Englund, 2006). However, only 35% of Tbr2+ UBCs expressed tdT,
109 suggesting that only a subpopulation of UBCs express tdT driven by Drd1 promoter activity (**Figure 1C,**
110 **Figure 1-S1**). Since two primary classes of UBCs have been previously characterized (Kim et al., 2012;
111 Zampini et al., 2016), we relied on known immunohistochemistry markers to characterize tdT+ UBCs. The
112 majority of tdT+ neurons express mGluR1 (**Figure 1D**) (71%, n=2 mice, 779 cells). The mGluR1+ and tdT+
113 populations do not completely overlap, as only 65% of mGluR1+ UBCs express tdT. Very few tdT+ UBCs
114 belong to calretinin+ (CR) type: 5.3% of tdT+ UBCs express CR, and 12.5% of CR+ UBCs express tdT
115 (**Figure 1E**). Given these data, we infer that in the Drd1-Cre;tdT cross, all cerebellar tdT+ cells are UBCs,
116 and that these tdT+ UBCs are a subset of the total UBC population, mostly comprised of mGluR1+ ON
117 UBCs. A prior report using a different Drd1-Cre mouse line reported the expression of Drd1 receptors in
118 deep cerebellar nuclei (Locke et al., 2018). In contrast, we do not see expression of tdT in the cerebellar
119 nuclei in this transgenic cross. Because Cre recombinase lines can show developmentally regulated
120 expression patterns, next we evaluated whether tdT+ UBCs contain Drd1a receptors using fluorescent in
121 situ hybridization (FISH) to label *tdT* and *Drd1a* mRNA transcripts. High density tdT transcripts were used
122 to create ROIs in a custom FIJI pipeline (Schindelin et al., 2012; Schneider et al., 2012) to examine
123 colocalization with *Drd1a* transcripts. We found that up to 76% of *tdT*+ (**Figure 1F**) UBCs expressed *Drd1a*
124 transcripts in low abundance (n=4 animals, 2553 cells) across an age range from P20s to P60s (**Figure 1-**
125 **S1B-C**). The density of *Drd1a* puncta was 40-fold enriched in the volume of *tdT*+ ROIs, compared to

126 regions outside the cell bodies (**Figure 1-S1D**). These data suggest that tdT+ UBCs express modest levels
127 of Drd1a receptors.

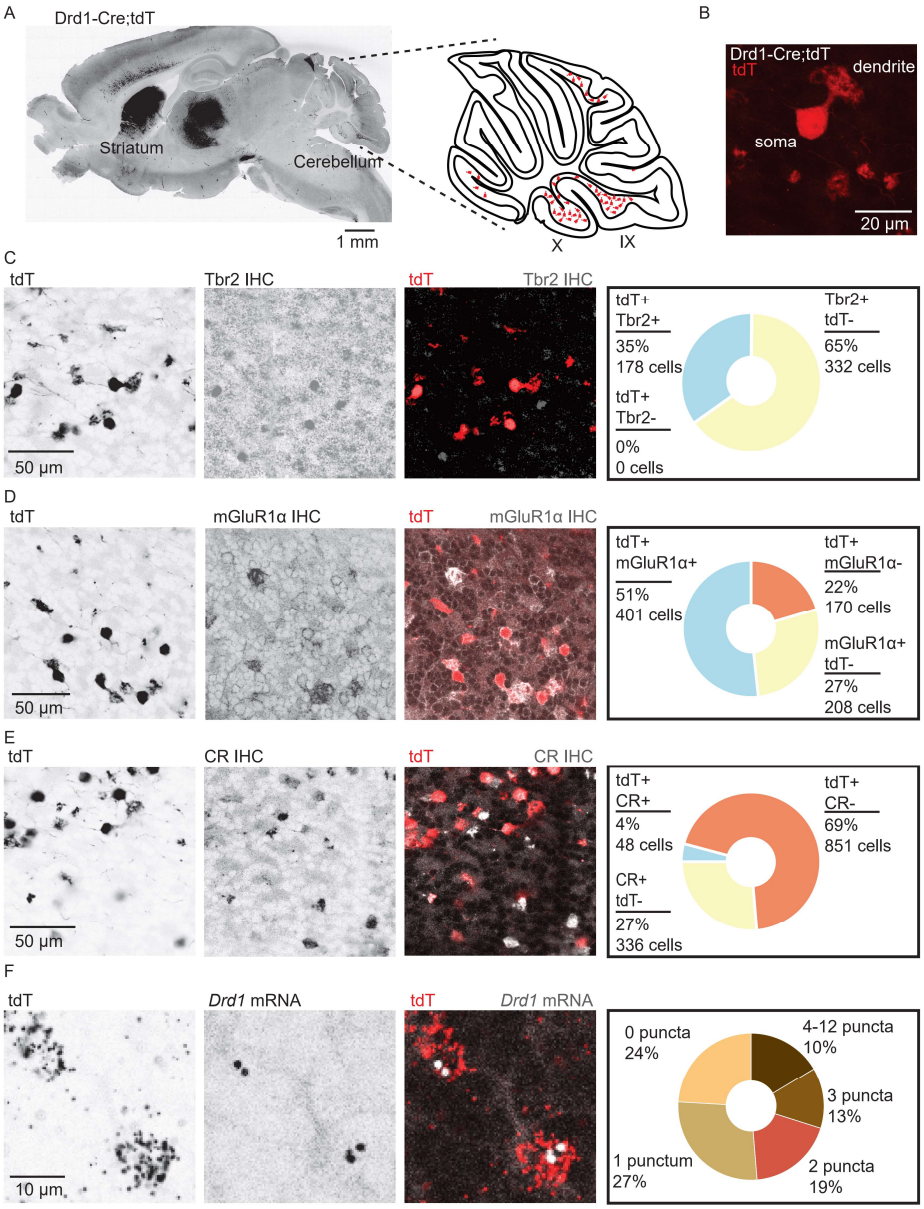

128

129 **Figure 1: Drd1 receptors are expressed in mGluR1+ UBCs.**

130 **A.** *Left*: A whole brain parasagittal section from a Drd1-Cre;tdT reporter cross. *Right*: A cartoon view of a parasagittal
131 slice of the cerebellar vermis. TdTomato expressing UBCs are abundant in lobules IX/X of the vermis. Scale bar, 1
132 mm.

133 **B.** A confocal image of a tdT+ UBC in the cerebellum of a Drd1-Cre mouse, showing the characteristic dendritic brush
134 morphology of a UBC. Scale bar, 20 µm.

135 **C.** *Left*: Confocal images of immunofluorescent labeling of Eomesidermin (Tbr2) in lobules IX/X of the cerebellar
136 vermis. *Right*: Pie chart describing overlap of cerebellar tdT+ cells and Tbr2. All tdT+ cells express Tbr2, and a
137 subpopulation (~35%) of Tbr2 cells expresses tdT (n=2 mice, 510 cells). Scale bar, 50 µm.

138 **D.** *Left:* Similar to **C**, but for mGluR1. *Right:* Out of all tdT+ UBCs 70% expressed mGluR1*,* 66% of mGluR1+ UBCs
139 were positive for tdT (n=2 mice, 779 cells). Scale bar, 50 µm.

140 **E.** *Left*: Similar to **C-D**, but for calretinin (CR). *Right:* labeling shows little overlap between CR and tdT+ UBCs, 5.3%
141 of tdT+ UBCS express CR, and 12.5% of CR+ express tdT (n=2 mice, 1235 cells). **C-D**. Inverted greyscale, single-
142 channel images; in merged images, red represents tdT signal, grey represents antibody labeling for Tbr2, mGlur1, or
143 CR, respectively. Scale bar, 50 µm.

144 **F.** *Left:* Sample confocal images of FISH, labeling *tdT* and *Drd1a* transcripts in cerebellar UBCs. Inverted greyscale
145 LUT is used for single-channel images. In merged images, red represents tdT signal, grey represents Drd1 labeling.
146 *Right*: The majority (~76%) of tdT+ UBCs express Drd1 transcripts (n=4 mice, 2553 cells). Scale bar, 10 µm.

---

147 **Functional characterization of Drd1a activation in UBCs**

148 To evaluate the consequences of Drd1a receptor activation we used current clamp recordings of tdT+
149 UBCs within lobules IX/X of the cerebellar vermis (**Figure 2A-F, Figure 2-S1A-D**). Puff application of
150 selective Drd1 agonist SKF81297 increased the firing rate of tdT+ UBCs (**Figure 2C-D**) (2.48 Hz increase,
151 110% increase from baseline, n=13 cells, paired Wilcoxon signed rank test, p=0.02). We also observed
152 increases in resting membrane potential and input resistance (**Figure 2F**). In a separate data set, we
153 applied SKF81297 in the presence of Drd1 antagonists SKF83566, SCH39166, and SCH23390, blocking
154 the increases in firing rate, membrane potential, and input resistance (**Figure 2E-F**) (n=13 cells, paired
155 Wilcoxon signed rank test, p=0.49). Puff application of ACSF likewise elicited no changes in firing rate
156 (n=13 cells, paired Wilcoxon signed rank test, p=0.33). Thus, UBCs respond to Drd1a activation with an
157 enhancement in activity, consistent with previous experiments on the effects of Drd1a activation in the
158 striatum and medial prefrontal cortex (mPFC) (Aosaki et al., 1998; Chen et al., 2007; Hernandez-Lopez et
159 al., 1997).

160 Prior research shows an increase in N-methyl-D-aspartate receptor (NMDAR) currents during the activation
161 of Drd1 receptors in mPFC neurons (Chen et al., 2004). Using electrical stimulation of mossy fibers, we
162 found an increase in peak amplitude of NMDAR currents after the flow in of 10 µM SKF81297 (**Figure 2I-K**)
163 (15% increase in peak current, n=9 cells, paired t-test, p=0.0251). These experiments were done in the
164 presence of blockers for fast neurotransmission, 1 µM NBQX, 1 µM gabazine, and 1 µM strychnine. In a
165 subset of experiments, we verified that the measured currents were fully blocked by the application of
166 NMDAR antagonist CPP (10 µM, n=5 cells) (**Figure 2-S1E**). Since UBCs are recurrently connected, the
167 increase in NMDAR currents may be due to a postsynaptic mechanism or a consequence of increased
168 excitability in presynaptic UBCs. To distinguish between pre- and post-synaptic mechanisms, we used two-
169 photon focal uncaging of MNI L-glutamate to bypass presynaptic terminals (**Figure 2L-M**) (Kozorovitskiy et

al., 2015; Xiao et al., 2018). In the presence of 1 mM MNI L-glutamate for uncaging, 1 μM TTX to silence spontaneous release, and drugs to isolate NMDAR currents, we uncaged glutamate near the dendritic brush of voltage clamped UBCs held at +40 mV. NMDAR mediated currents in response to 1 ms long pulses of 725 nm laser light were compared for experiments with and without 10 μM SKF81297. Current amplitudes increased with Drd1 activation, suggesting a post synaptic mechanism of action (**Figure 2 N-O**) (51% increase of average amplitude, n=13 cells, unpaired t-test, p=0.0068). These experiments support an NMDAR-mediated component to Drd1 activation in UBCs, although given findings from striatum and mPFC it is likely that additional mechanisms account for changes in excitability we have observed (Gorelova and Yang, 2000; Surmeier and Kitai, 1993).

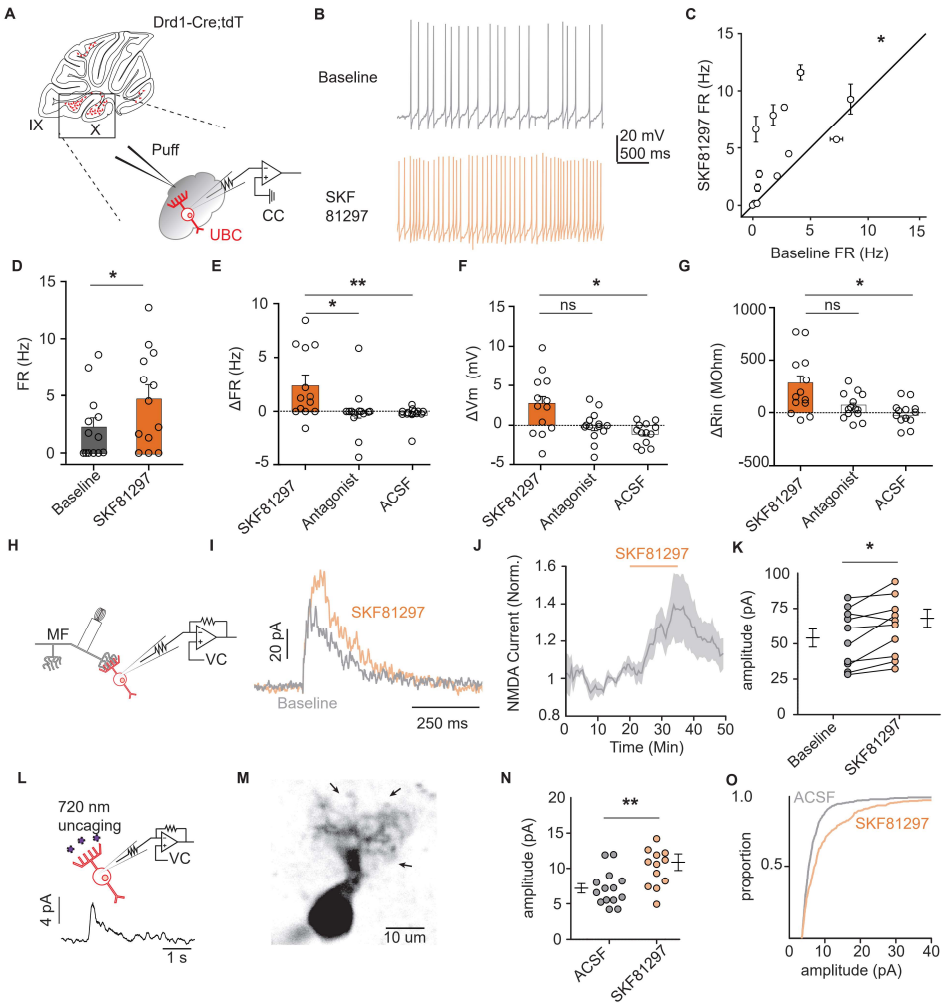

Figure 2. Drd1 activation increases the firing rate and NMDAR currents in UBCs.

A. Diagram of experimental setup with tdT+ UBCs recorded in whole-cell current clamp configuration. Firing rate was measured during baseline period, followed by application of Drd1 agonist SKF81297 (500 μM) with 300 ms-long puffs from a proximally located pipette.

B. Voltage traces from an example cell which increased its firing rate in response to SKF81297 application.

185 **C, D.** Group comparison, mean firing rates during the baseline period and application of SKF81297 (n=13 cells, paired
186 Wilcoxon signed rank test, p=0.02, *p<0.05).

187 **E-G.** Changes in firing rate (FR) in **E**, resting membrane potential (mV) in **F**, and input resistance (Rin) in **G**. The
188 SKF81297 group, as in in **C-D**. Comparisons are between three independent data sets. Antagonist group: SKF81297
189 was applied in the presence of Drd1 blockers 1 μM SKF83566, 1 μM SCH39166, and 1 μM SCH23390. ACSF group:
190 puff application ACSF instead of SKF81297 (Kruskal-Wallis test, FR p=0.0044, Vm p=0.0024, Rin p=0.02; Dunn's
191 multiple comparison test, *p<0.05, **p<0.01).

192 **H.** Schematic of experimental setup. Voltage clamp recordings were performed in tdT+ UBCs, paired with stimulation
193 mossy fiber inputs to evoke NMDA receptor mediated currents (inter-trial interval, ITI, 5 seconds), in the presence of
194 blockers for AMPA, GABA and glycine receptors (1 μM NBQX, 1 μM gabazine, 1 μM strychnine).

195 **I.** Sample traces show an increase in NMDAR current amplitudes during the application of SKF81297.

196 **J.** Trace of normalized peak amplitude of NMDAR currents across cells (n=10 cells). Shaded region, ±SEM.

197 **K.** Summary plot of average evoked NMDAR current amplitudes before and after application of 10 μM SKF81297
198 (n=10 cells, paired t-test, p=0.0251).

199 **L.** *Top:* Schematic of two-photon uncaging MNI-L-glutamate uncaging experiments. TdT+ UBCs were voltage-
200 clamped and imaged using a two-photon laser scanning microscope. Laser pulses (725 nm) directed near the
201 dendritic brush (10-20 mW, 1 ms, 60 s ITI) were used evoked NMDAR mediated currents. *Bottom:* Example current
202 trace.

203 **M.** Two-photon imaging Z-projection of a tdT+ UBC. Arrows represent separate uncaging site locations. Scale bar, 10
204 μm.

205 **N.** NMDAR current amplitudes in ACSF vs 10 μM SKF81297 (unpaired t-test, p=0.0068, **p<0.01). Each data point is
206 the average amplitude of NMDAR currents evoked by glutamate uncaging from one cell (ACSF n=14 cells, SKF81297
207 n=13 cells).

208 **O.** Cumulative distribution of uncaging-evoked NMDAR current peak amplitudes for ACSF and SKF81297 groups.

---

209 **Defining the source of cerebellar DA**

210 Three TH+ populations are poised to serve as the source of DA to the cerebellum based on prior data: the
211 midbrain dopaminergic cells of the Substantia Nigra pars compacta (SNc) and the Ventral Tegmental area
212 (VTA), local TH+ Pkj cells of the cerebellum (Takada et al., 1993), and nearby locus coeruleus (LC)
213 neurons that release DA as well as norepinephrine in other brain regions (Takeuchi et al., 2016). First, to
214 evaluate whether Drd1+ UBCs could receive inputs from midbrain DA neurons, we carried out retrograde
215 tracing from lobules IX/X of the vestibulo-cerebellum in a Dat-Cre;tdT mouse cross. We found no support
216 for the existence of this projection (**Figure 3A-C**), despite the abundance of Dat-Cre;tdT axonal fibers in
217 the cerebellum (**Figure 3B**, inset). Retrograde labelling confirmed that these tdT+ axons originate from a

218 pre-cerebellar brainstem nucleus, the lateral reticular nucleus (LRN), and not the SNc/VTA. LRN neurons
219 are glutamatergic, forming mossy fiber rosettes within the cerebellum (Rajakumar et al., 1992; Wu et al.,
220 1999). There are no prior reports of LRN expressing proteins required for DA synthesis or packaging. To
221 evaluate the expression of transcripts required for DA release, we performed FISH labeling of LRN neurons
222 and found that few neurons express mRNA for either tyrosine hydroxylase or vesicular monoamine
223 transporter type 2 *(Vmat2/Slc18a2*) (n=3 mice, *Th*,19/135 LRN cells, *Vmat2* 2/135 LRN cells) (**Figure 3-**
224 **S1B-D**).

225 Next, using FISH and antibody labeling, we confirmed previous reports of TH expression in Pkj cells of
226 vermal lobules IX and X (**Figure 3D-F, Figure 3-S1A**) (Austin et al., 1992; Sakai et al., 1995; Takada et al.,
227 1993). Despite the presence of *Th*, these neurons lacked the transcripts for Dopa Decarboxylase (*Ddc*), the
228 enzyme responsible for converting L-DOPA to dopamine (**Figure 3E-F**) (n=2 mice, 163 cells). Similarly, we
229 found minimal expression of *Vmat2* or dopamine active transporter *(Dat/Slc6a3*), in contrast to *Th*+
230 neurons of the SNc (**Figure 3D, F**). Thus, DA release from TH+ Pkj cells is unlikely. Exclusion of the first
231 two hypothesized DA sources left the nearby monoaminergic LC as a candidate. To verify that the LC
232 projects specifically to cerebellar regions enriched in Drd1+ UBCs, we used a TH-Flpo mouse line. We
233 injected a retrograde AAV (AAV2/retro-CAG-fDIO-Cre-EGFP) into lobules IX/X and found EGFP+ LC
234 neurons (**Figure 3G**). Consistent with TH expression in lobule IX/X (**Figure 3D-E, Figure 3-S1A**), local Pkj
235 cells were also labelled by the injection. The SNc and VTA did not express EGFP, further confirming the
236 absence of a TH+ projection from VTA/SNc. Given these data, the most likely source of dopamine to the
237 Drd1+ UBCs is the LC.

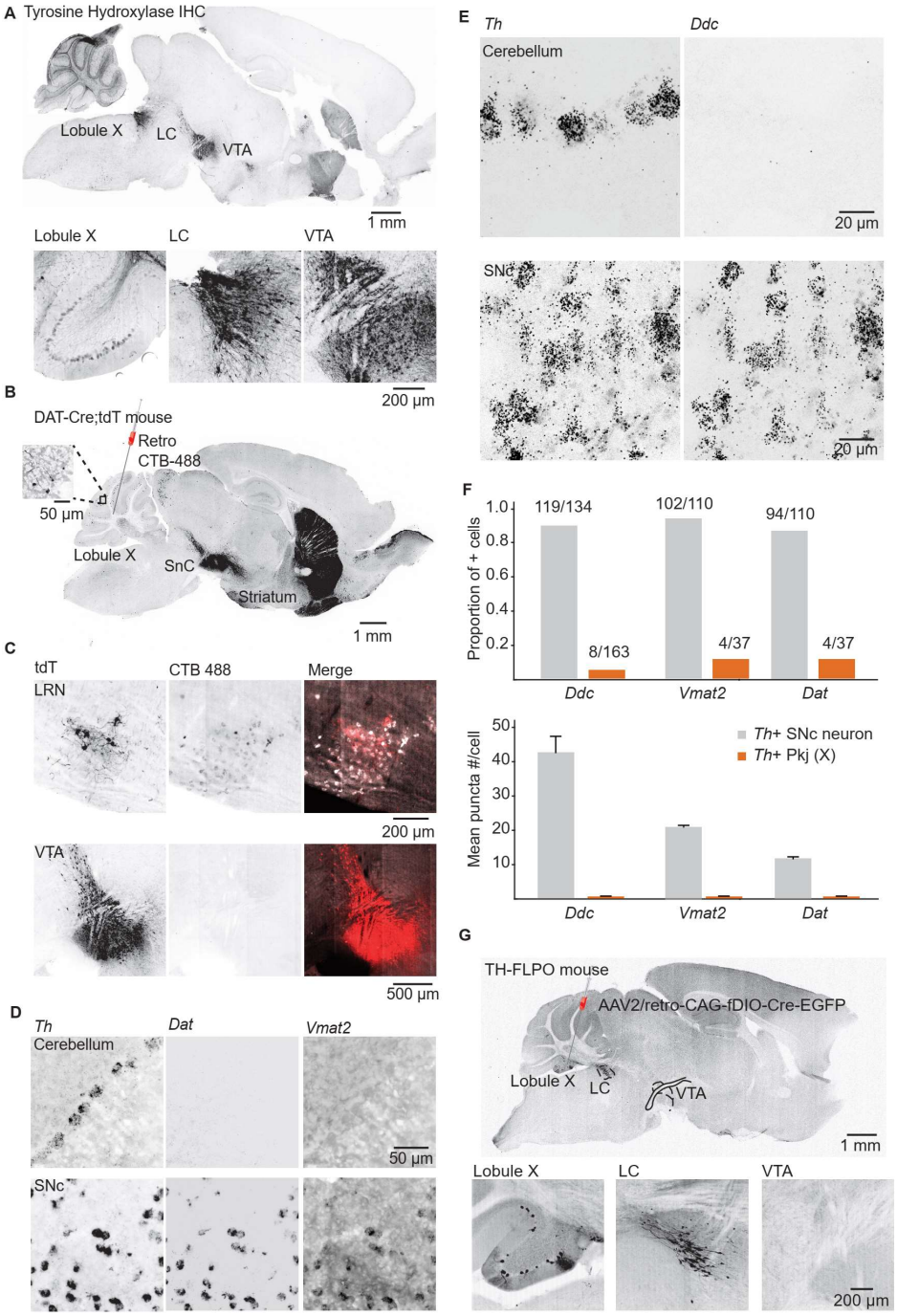

Figure 3. Interrogating potential dopamine sources for cerebellar lobules IX/X.

A. *Top:* Parasagittal slice of a mouse brain immunolabelled for tyrosine hydroxylase (TH). Three hypothesized sources of dopamine include Purkinje cells in lobule X of the vermis, locus coeruleus neurons, and VTA DA neurons. Scale bar, 1 mm. *Bottom:* Close-up of regions of interest. Scale bar, 200 µm.

B. Example retrograde labeling experiment with CTB-488 injected into the cerebellum of a Dat-Cre;tdT reporter mouse (n=3 mice). Scale bar, 1 mm. *Inset:* TdTomato expressing cerebellar fibers are morphologically consistent with mossy fiber terminals and are restricted to the granule layer. Scale bar, 50 µm.

246 **C.** Close-up images from a retrograde CTB-488 injection. No labeling is observed in the tdT+ neurons in the ventral
247 tegmental area (VTA), in contrast to tdT+ neurons in the lateral reticular nucleus (LRN), a glutamatergic pre-cerebellar
248 brainstem nucleus. Scale bars, 200 µm and 500 µm.

249 **D.** *Top*: Confocal images of FISH labeling for *Th* and *Ddc* transcripts in Pkj cells in lobule X. *Bottom*, images of SNc
250 neurons co-labeled for *Th* and *Ddc* transcripts (n=2 mice). Scale bar, 20 µm.

251 **E.** Comparison of TH+ Pkj cells and SNc neurons co-labeled for dopamine active transporter *(Dat)* and vesicular
252 monoamine transporter type 2 *(Vmat2)* (n=2 mice). Scale bar, 50 µm.

253 **F.** Quantification of transcripts involved in synthesis and release of DA. *Top*: Few TH+ Pkj cells express transcripts for
254 *Ddc, Vmat2* or *Dat*. *Bottom*: The few TH+ Pkj cells that express *Ddc, Vmat2*, and *Dat* express low transcript numbers
255 in comparison to SNc neurons (n=2 mice). Grey bars represent counts from SNc DA neurons, red bars represent *Th*+
256 Pkj cells.

257 **G.** *Top*: Parasagittal section from a TH-Flpo mouse injected with retrograde Flp-dependent virus expressing GFP
258 (AAV2/retro-CAG-fDIO-Cre-EGFP). Scale bar, 1 mm. *Bottom*: Close-up of regions of interest. No GFP labeling of
259 VTA/SNc neurons was observed, in contrast to LC neurons and local TH+ Pkj cells that were retrogradely labeled by
260 GFP (n=2 mice). Scale bar, 200 µm.

---

261 **Tracing inputs of Drd1+ UBCs using trans-synaptic pseudo-typed rabies virus**

262 To assay dopaminergic presynaptic inputs to UBCs we performed trans-synaptic tracing with a modified
263 rabies virus CVS-N2cΔG (Reardon et al., 2016) which allowed us to label all presynaptic partners of
264 neurons expressing Cre recombinase (**Figure 4A**). The modified rabies construct cannot enter cells that do
265 not express a TVA receptor and lacks the glycoprotein necessary to replicate into mature virus that can
266 travel pre-synaptically. We infected UBCs with both TVA and the glycoprotein by injecting AAVs (AAV1-
267 CAG-Flex-H2B-eGFP-N2cG and AAV1-EF1α-FLEX-GT) into a Drd1a-Cre transgenic mouse line. After 4-6
268 weeks of expression, we injected the modified rabies virus into the same region of the cerebellum. The
269 rabies virus travels monosynaptically to the pre-synaptic partners of local UBCs. Histology was carried out
270 after 7-8 days of rabies virus expression. The rabies virus includes a transgene for tdTomato, and the AAV
271 viruses contains a GFP tag. UBCs initially infected with rabies express both GFP and tdT, while cells
272 presynaptic to the starter cells express only tdT. To analyze these data, we used FIJI based scripts
273 (Schindelin et al., 2012) to quantify the number of UBC starter cells and their presynaptic partners after
274 immunohistochemistry to enhance GFP and tdT fluorescence. We did not dissect semicircular canals or
275 otoliths, so they are not included in this analysis, although previous research shows that semicircular
276 canals project directly to mGluR1+ UBCs (Balmer and Trussell, 2019). Our data (n=4 mice, starter cells
277 33.5±3.9/mouse) show presynaptic labelling of Pkj cells, Golgi cells, cerebellar nuclei neurons, vestibular
278 nuclei neurons, and a sparse population of LC neurons (**Figure 4B-E**). We did not find any labeling in the
279 midbrain dopaminergic nuclei, even though input tracing using pseudo-typed rabies viral vectors has been
280 previously used to label monoaminergic inputs (Schwarz et al., 2015; Wall et al., 2013). It is unknown
281 whether rabies virus labels certain presynaptic inputs preferentially based on properties such as firing

282 rates, axonal length and structure, or neurotransmitter identity (Rogers and Beier, 2021). The majority of
283 inputs are from nearby cerebellar nuclei cells, consistent with prior reports on their projections back to
284 cerebellar cortex (Houck and Person, 2015; Judd et al., 2021). Despite low numbers of starter cells, we
285 found sparse labeling of neurons in the LC. These findings are consistent with our anatomical tracing using
286 retro-AAV (**Figure 3G**), confirming the LC as the likely source of DA for Drd1+ UBCs.

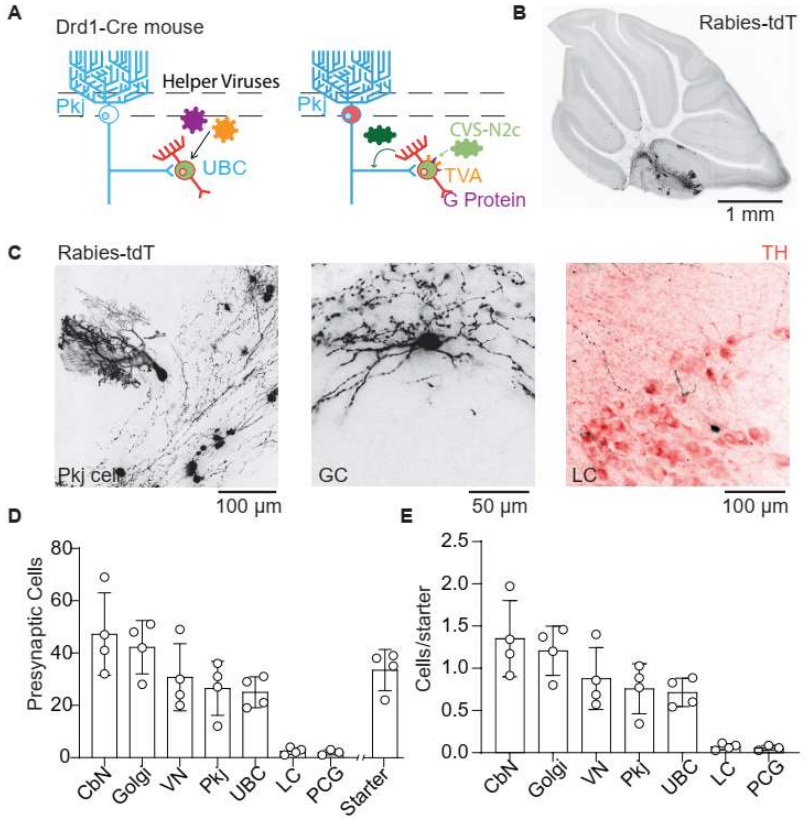

287

288 **Figure 4. Trans-synaptic tracing of Drd1+ UBC inputs.**

289 **A.** Cartoon of viral expression for trans-synaptic modified rabies virus tracing. Helper AAV virus expressing two Cre
290 dependent constructs, TVA receptors and glycoprotein. After 4-6 weeks of helper virus expression in UBCs we
291 injected modified rabies (CVS-N2cΔG). The rabies virus only enters UBCs expressing the TVA receptor. Once
292 expressed in a UBC along with the glycoprotein, the virus can create a functional capsid and travel pre-synaptically.

293 **B.** Representative image of sagittal cerebellar slice. Cells infected with rabies virus are labelled with tdTomato. Scale
294 bar, 1 mm.

295 **C.** Example cells presynaptic to Drd1+ UBCs labelled with tdTomato. *Left:* Pkj Cell, *Center*: Golgi cell (GC). *Right:* LC
296 neuron labeled with tdT from rabies virus and TH antibody labeling. Scale bars, 50 and 100 µm.

297 **D.** Number of cells labelled by CVS-N2cΔG rabies virus (n=4 mice). In addition to UBCs, Pkj cells, and Golgi cells, we
298 found tdT labeled cells in the cerebellar nuclei (CbN), vestibular nuclei (VN), pontine central grey (PCG), and locus
299 coeruleus (LC). Starter cells indicate the number of UBCs co-labeled with GFP from helper AAVs and rabies virus
300 driven tdT.

301 **E.** Quantification of labeled presynaptic cells normalized to the number of starter UBCs.

302 **Optical measurements of monoamine release from LC fibers onto UBCs**

303 To obtain evidence for functional DA release in the cerebellum, we turned to optical dopamine sensors that
304 can directly measure dopamine dynamics with more sensitivity than fast scan cyclic voltammetry and
305 higher temporal resolution than microdialysis (Patriarchi et al., 2018; Sabatini and Tian, 2020). We injected
306 a Cre-dependent version of $GRAB_{DA2h}$ AAV (Sun et al., 2018, 2020) into lobule IX/X of the cerebellum of
307 Drd1a-Cre animals. We then paired electrical stimulation of cerebellar cortical inputs with 2-photon imaging
308 of $GRAB_{DA2h}$ fluorescence in UBCs in the acute slice (**Figure 5A-B**). We found that electrical stimulation of
309 inputs to lobule X (50 stimuli, 50 Hz) elicited an increase in $GRAB_{DA2h}$ fluorescence in UBCs (**Figure 5C**).
310 This increase could be blocked by bath application of Drd2 antagonist, as expected for this sensor (**Figure**
311 **5D**) (1 μM L-741,626, n=10 cells, 4.88-fold reduction in peak amplitude, paired t-test, p=0.002). In a subset
312 of experiments, we validated the maximal response $GRAB_{DA2h}$ by bath applying Drd2 agonist (1 μM
313 quinpirole) (**Figure 5-S1B**). The electrical stimulation protocol lacks specificity, activating all inputs into
314 lobule X. To selectively activate the putative DA inputs, we crossed Drd1-Cre and TH-Flpo mouse lines to
315 express $GRAB_{DA2h}$ in UBCs and ChR2 in TH+ inputs to the nodulus (**Figure 5E**). We confirmed that our
316 injection of AAV1-Flex-FRT-ChR2-mCherry into the LC labelled axons across the entire cerebellum,
317 including the regions which contain Drd1+ UBCs (**Figure 5F, Figure 5-S1A**). We imaged $GRAB_{DA2h}$
318 fluorescence in UBCs in the acute slice while optogenetically activating LC axons (200 pulses, 39 Hz, 2 ms
319 pulses, 460 nm). In each experiment, the absence of TH+ Pkj cell labeling was confirmed to ensure
320 selective LC targeting without overflow of ChR2 expression into the cerebellum. We found time-locked
321 increases of $GRAB_{DA2h}$ fluorescence in UBCs in response to optical stimulation in a subset of UBCs (n=2
322 mice, 5/20 cells) (**Figure 5G-H**). Optically evoked $GRAB_{DA2h}$ transients had an average success rate of
323 ~40% across responding cells. Responses to stimulation were bimodal, exhibiting either a substantial
324 change in fluorescence (>0.1 F/F), or no detectable change (**Figure 5G-H**). As a control we interleaved
325 trials where we did not deliver optogenetic stimulation. Altogether, these electrical and optical imaging
326 experiments suggest that LC axons release monoamines onto UBCs in lobules IX/X of the cerebellar
327 vermis.

328 **Electrophysiological recordings of DA release from LC fibers**

329 $GRAB_{DA}$ is preferentially activated by dopamine, but it maintains a slight sensitivity to norepinephrine (DA
330 EC_{50}=0.13 μM, NE EC_{50}=1.7 μM) (Sun et al., 2020). To evaluate whether release of dopamine from LC
331 fibers can activate Drd1 receptors on UBCs we performed acute slice electrophysiology. Since Drd1
332 receptors activate $G\alpha_s$-coupled protein cascades (Stoof and Kebabian, 1984; Surmeier and Kitai, 1993),
333 and whole-cell recordings can dialyze cytosolic proteins involved in G protein-coupled receptor (GPCR)
334 signaling (Lahiri and Bevan, 2020), we decided to use cell-attached recordings to measure potential effect
335 of dopamine release from LC axons. First, we performed cell attached recordings of Drd1+ UBCs, collected

336 data during a baseline period and then applied 10 μm SKF81297 (**Figure 5I**). Consistent with our whole
337 cell current clamp recordings, we measured an increase in spontaneous firing rate in tdT+ UBCS in
338 response to Drd1 agonist (**Figure 5J**) (n=10 cells, paired Wilcoxon signed rank test, p=0.002). These flow-
339 in data act as a benchmark for the following experiments where we optogenetically stimulate LC fibers
340 using a Drd1-Cre; Th-Flpo cross transgenic line (**Figure 5K**). We aimed for maximal pharmacological
341 isolation of DA signaling in these experiments, using a cocktail of receptor antagonists. To avoid activating
342 alpha- or beta-adrenergic receptors with LC stimulation (although their expression in UBCs specifically has
343 not been examined), we applied alpha (10 μM prazosin) and beta (10 μM propranolol) adrenergic receptor
344 antagonists. Additionally, since LC neurons have been shown to release glutamate (Fung et al., 1994;
345 Yang et al., 2021), we blocked AMPAR and NMDAR-mediated excitatory neurotransmission using NBQX
346 (5 μM) and CPP (10 μM). Notably, the blockade of NMDA receptors would be expected to abolish a fraction
347 of Drd1 activation effects (based on our results in **Figure 2H-O**), providing a strong test of the existence of
348 additional mechanisms altering cellular excitability in UBCs downstream of Drd1 stimulation. GPCR
349 cascades have many downstream targets, and so it is not surprising that several mechanisms could be
350 responsible for changes in firing rate. TRPC3 channels were blocked using Pyr-3 (1 μM), to avoid
351 glutamate opening TRPC3 channels through mGluR1 activation (Borges-Merjane and Trussell, 2015). Pkj
352 cells express adrenergic and Drd2 receptors (Basile and Dunwiddie, 1984; Cutando et al., 2019; Kim et al.,
353 2009; Lippiello et al., 2015); to avoid polysynaptic effects from the release of NE or DA from LC fibers we
354 blocked fast inhibitory transmission using gabazine (10 μM) and strychnine (1 μM). For these experiments,
355 to minimize depletion of neurotransmitter from the LC axons, stimulation was delivered at 20 Hz with a 60
356 second inter-stimulus interval. We measured a small but significant increase in the firing rate of Drd1+
357 UBCs in response to LC fiber stimulation (**Figure 5J**) (1.2 Hz increase, 26% increase from baseline, n=8
358 cells, paired Wilcoxon signed rank test, p=0.02). In a separate set of experiments with Drd1 antagonist (5
359 μM SCH39166) present in the bath, we measured no statistically significant changes in firing rate.

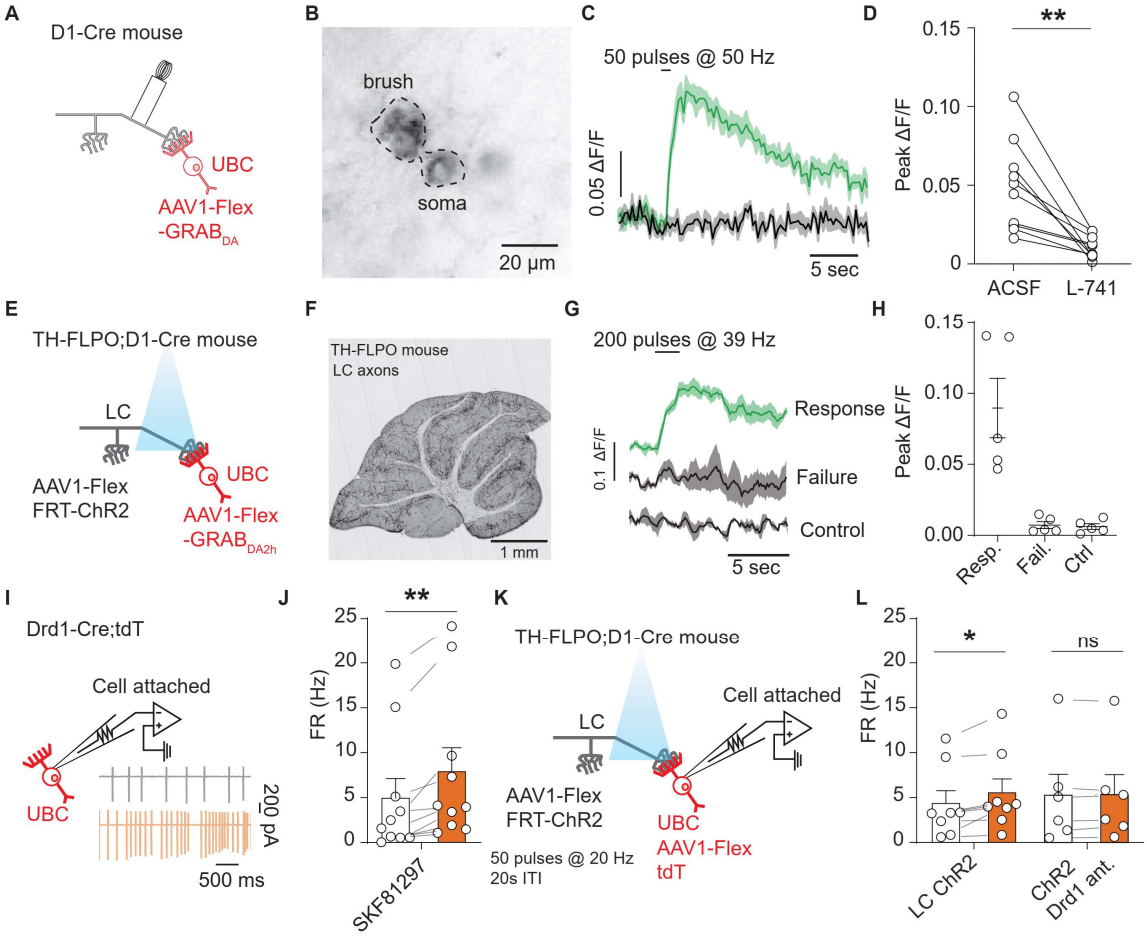

Figure 5. LC fibers release DA in the cerebellum activating UBC Drd1 receptors.

A. Schematic of experimental setup, Cre-dependent GRAB$_{DA2h}$ expressed in UBC, with a monopolar electrode placed in the white matter of Lobule X.

B. Two-photon image of UBCs expressing Cre-dependent GRAB$_{DA2h}$ in a Drd1-Cre cerebellum.

C. Sample trace from one cell (5 trial average) in response to electrical stimulation before and after application of Drd2 antagonist (1 µM L-741,626). Shaded regions, SEM.

D. Group data of peak amplitude of ΔF/F in response to 50 Hz stimulation of axonal cerebellar input before and after flow in of Drd2 antagonist (1 µM L-741,626) (n=10 cells, paired t-test, p=0.002, **p<0.01).

E. Experimental design using dual virus injection to express ChR2 (Flpo-dependent) in LC axons and GRAB$_{DA2h}$ (Cre-dependent) in UBCs. Light pulses were delivered with 460 nm LED (2 ms pulse width, 200 pulses, 39 Hz).

F. Anterograde labeling of axons from the LC to the cerebellum. Image from an injection of AAV1-FLEX-FRT-ChR2-mCherry into the LC shows axons spreading broadly across all layers of the cerebellum (n=2 mice). Scale bar, 1 mm.

G. Sample traces of the changes in GRAB$_{DA2h}$ fluorescence in response to optical activation of ChR2+ LC axons from a single cell. The three traces correspond to trials with an evoked response, trials with no response, and control trials where no light stimulation was given. Lines represent the mean of 3 trials, shaded regions are ±SEM.

376 **H.** Summary data from several experiments, 5/20 cells responded to optogenetic activation (6 acute slices, n=2 mice).
377 Error bars represent SEM.

378 **I.** Diagram of experimental setup, with tdT+ UBCs recorded in a cell-attached recording configuration. *Inset:* Traces
379 from an example cell showing action potential recordings before (black) and after (orange) bath application of 10 μM
380 SKF81297.

381 **J.** Summary data from cell-attached recordings before (white) and after (orange) the application of a Drd1 agonist.
382 (n=10 cells, paired Wilcoxon signed rank test, p=0.002, **p<0.01).

383 **K.** Schematic of cell-attached recordings paired with selective optogenetic activation of LC fibers. After a baseline
384 period light stimuli were delivered every 20 seconds (460 nm, 50 pulses, 20 Hz, 1 ms pulse width).

385 **L.** Mean firing rates before (white) and during (orange) optogenetic stimulation period. *Right*, same but with Drd1
386 antagonist in the bath.

---

387 **Activation of UBCs can pause Pkj cell firing**

388 In order to evaluate the function of Drd1+ UBCs within Lobule X of the cerebellar vermis we transfected
389 Drd1-Cre mice with ChR2-EYFP AAV virus (AAV5-EF1a-DIO-ChR2-eYFP) and performed cell attached
390 recordings from Pkj cells (**Figure 6A-B**). We stimulated UBCs with a train of LED pulses (460 nm, 10 Hz,
391 50 pulses, 1 ms pulse width). Each pulse caused a small burst of action potentials (2-5 APs). UBCs were
392 more likely to respond with multiple spikes to a pulse at the beginning of the train than at the end (**Figure**
393 **6B-C**). Pkj cells did not significantly alter their average firing rate on trials with optogenetic stimulation
394 (**Figure 6D**). However, in a subset of Pkj cells, stimulation caused a brief pause in firing during the 500 ms
395 period after the beginning of the optogenetic stimulus (**Figure 6E**). Firing rate was normalized using a z-
396 score. If a cell's firing changed by 0.5 z-score SD during the 500 ms period after initial pulse, it was
397 considered changing. Cells were classified into 'Bursters', 'Pausers', or 'No response'. The majority of Pkj
398 cells (18/28) did not significantly change their firing rate, ~28% of cells were 'Pausers' (8/28) and 7% of Pkj
399 cells qualified as 'Bursters' (2/28) (**Figure 6F-G**). In a separate group of cells, we performed tight seal
400 recordings from Pkj cells and measured their responses to 5 pulses of optogenetic activation of UBCs.
401 Immediately afterwards, we broke into the cell and recorded EPSCs (-70 mV) and IPSCs (0 mV) in whole
402 cell voltage clamp mode (**Figure 6H**). We calculated the EPSC/IPSCs charge ratio and plotted it against
403 change in firing rate z-score (**Figure 6I**). Neurons with lower EPSC/IPSC ratios were more likely to pause
404 after the onset of stimulation, suggesting that in these cells the relatively larger inhibitory current favored
405 the pause. These data demonstrate that simultaneous activation of Drd1+ UBCs induces a decrease in Pkj
406 cell firing.

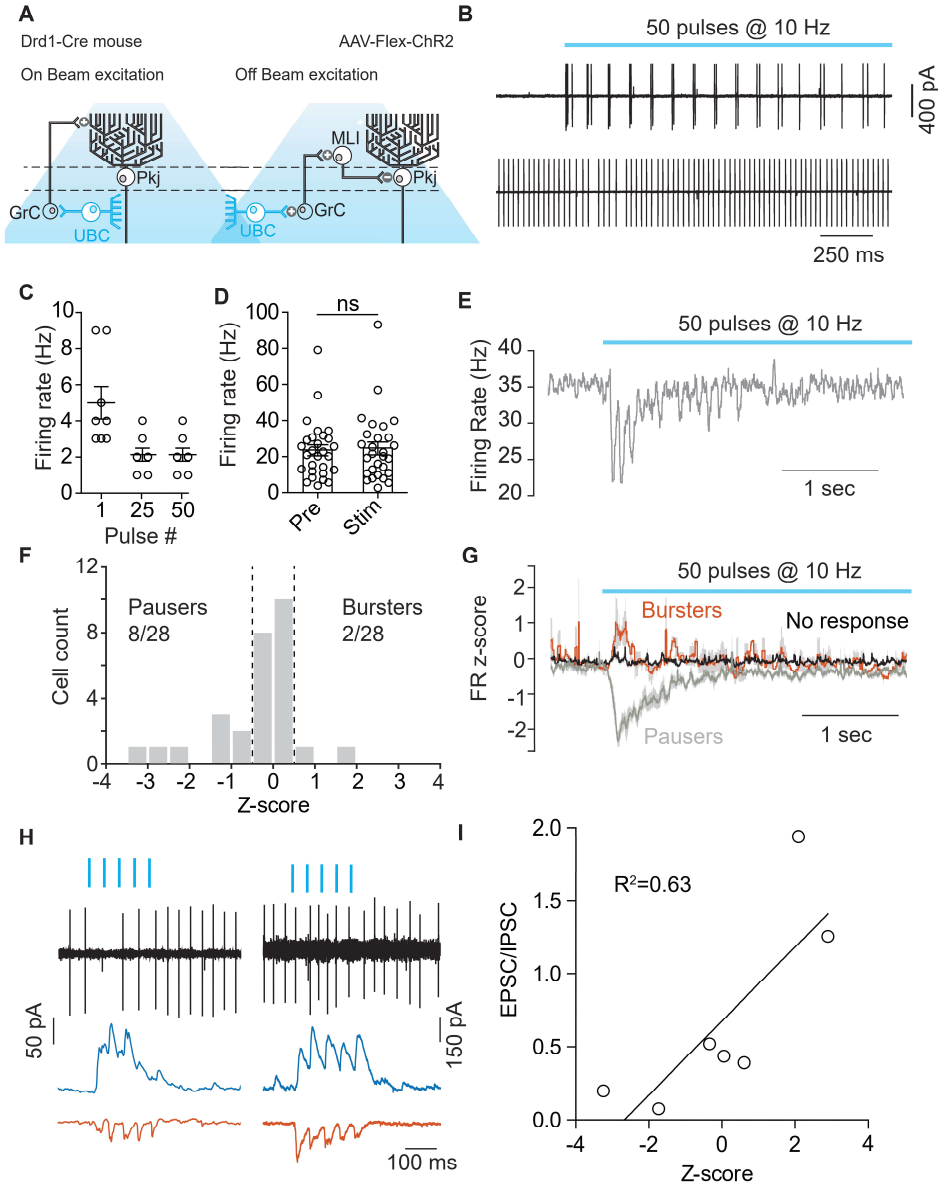

Figure 6. Optogenetic activation of UBCs can modulate Pkj cell activity.

A. Diagram of experimental setup highlighting the two pathways (On-beam, Off-beam) through which UBCs can modulate Pkj cell firing. Cre-dependent AAV5-EF1a-DIO-ChR2-eYFP was expressed in UBCs using a Drd1-Cre mouse line. Pkj cells were recorded in cell-attached and/or whole-cell voltage clamp configuration.

B. *Top:* Example trace from a cell-attached recording of a ChR2+ UBC which increased its firing rate during light stimulation (460 nm, 10 Hz, 50 pulses, 1 ms pulse width). *Bottom:* Cell attached recoding from Pkj cell.

C. The number of action potentials evoked in ChR2+ UBCs by a train of light pulses in response to the 1st, 25th and 50th individual pulse (n=8 cells).

D. A comparison of average firing rate of Pkj cells for trials before optogenetic stimulation of UBCs (Pre) and for trials with optogenetic activation (Stim) shows no significant difference.

418 **E.** The average firing rate (5 trials) of a single Pkj cell during the activation of nearby UBCs. Example cell transiently
419 decreased its firing rate in response to UBC activation.

420 **F**. Histogram of average z-scores of firing rates during the 500 ms period following the first optogenetic pulse.
421 Dashed lines indicate cut-off for categorization of response as either 'Burster' z-score > 0.5 or 'Pauser' z-score < -0.5.

422 **G.** Average z-score of firing rates across cells. 'Pausers' (n=8 cells) indicates data for cells that had z-score < -0.5,
423 'Bursters' (n=2 cells) indicates data for cells that had z-score>0.5, 'No response' (n=20 cells) include all other cells.
424 Shaded regions represent SEM.

425 **H.** Cell-attached and postsynaptic current recordings from example Pkj cells; *left* 'Pauser', *right* 'Burster'. Top traces
426 show cell-attached recordings before break-in. After break-in IPSCs (blue trace) and EPSCs (red) were recorded.

427 **I.** Firing rate z-score after optogenetic activation of UBCs plotted against EPSC/IPSC total charge ratio. Data show a
428 correlation between relative inhibitory input and pausing in Pkj cells (Linear regression, R^2=0.63, $F_{1,5}$=8.82, p=0.0312).

---

429 **Lobule X Pkj cells directly inhibit UBCs**

430 Previous work showed that in the vestibulo-cerebellum Pkj cells make inhibitory connections with nearby
431 granular cells (Guo et al., 2016). This connection has implications for how Pkj feedback can alter the
432 activity of their own inputs. Given the high density of UBCs in these same regions and the labeling of Pkj
433 cells in our presynaptic rabies virus tracing (**Figure 4B-E**), we evaluated the possibility of direct synaptic
434 connectivity between Pkj cells and UBCs. We used the Drd1-Cre mouse-line to label UBCs with a flexed
435 GFP reporter virus and selectively activated Pkj cells using a viral vector expressing ChR2-mCherry, driven
436 by the Pcp2 promoter (El-Shamayleh et al., 2017) (**Figure 7A**). We used epifluorescence to target and
437 patch UBCs with a high chloride ion concentration internal solution. This allowed us to measure IPSCs
438 (**Figure 7B, F**) while holding cells at -80 mV. $GABA_A$ currents were isolated using pharmacological blockers
439 of AMPA, NMDA, glycine and $GABA_B$ receptors (5 μM NBQX, 2 μM CPP, 1 μM strychnine, 1 μM
440 CGP54626). In order to distinguish between direct inhibition from Pkj cells and any indirect inhibition from
441 nearby Golgi cells, an mGluR2 agonist was included in the bath to silence Golgi cells (2 μM LY354740)
442 (Guo et al., 2016; Watanabe and Nakanishi, 2003). To verify that the LED stimulation protocol effectively
443 drove Pkj cell activity we performed cell attached recordings. We could reliably increase Pkj cell firing rate
444 during light stimulation (n=8 cells, 71 Hz +/- 6.7) (**Figure 7C**). In UBC voltage clamp experiments we found
445 that 11/24 UBCs received short latency synaptic input from Pkj cells (**Figure 7D**). Cells with successful
446 evoked IPSCs had a per trial success ratio of 0.64 on average (**Figure 7D**). There was significant variability
447 in the amplitude (91 pA, +/- 24) (**Figure 7H**) and timing (9.4 ms +/-2.4) (**Figure 7E**) of optically evoked
448 IPSCs, with some cells exhibiting large currents over the entire stimulation period and others responding
449 with a single large IPSC at the onset of stimulation. However, many UBCs exhibited short latency IPSCs in
450 response to stimulation of Pkj cells (**Figure 7E-F**), on the background of minimal spontaneous IPSCs
451 (**Figure 7-S1A**). In a subset of UBCs (n=9 cells) (**Figure 7F-G**) we flowed in 10 μM gabazine to ensure the

452 measured currents were due to $GABA_A$ channel opening. Application of gabazine abolished all evoked
453 currents (**Figure 7H**).

454

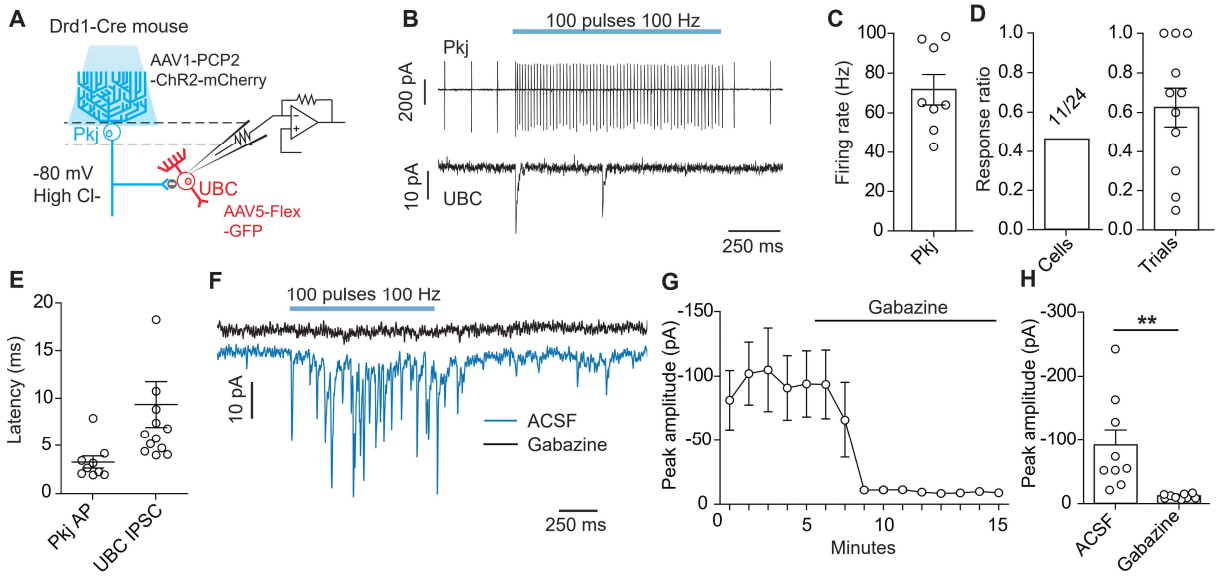

455

456 **Figure 7. Optogenetic activation of Pkj cells evokes short-latency IPSCs in UBCs.**

457 **A**. Diagram of experimental setup. Using a Drd1-Cre mouse line a Cre-dependent GFP was expressed in UBCs, Pkj
458 cells were transfected with AAV-Pcp2-ChR2-mCherry. UBCs recorded in whole-cell voltage clamp configuration.
459 Experiments were done with 5 μM NBQX, 2 μM CPP, 1 μM Strychnine, 1 μM CGP54626, 2 μM LY354740 in the bath.

460 **B.** *Top:* Example trace from a cell-attached recording of a mCherry+ Pkj cell which increased its firing rate during light
461 stimulation (460 nm, 100 pulses, 100 Hz, 0.5 ms pulse width). *Bottom:* Voltage clamp recording of UBC IPSCs.

462 **C.** Average firing rate of Pkj cells during light stimulation (n=8 cells).

463 **D.** Ratio of successful IPSC responses. *Left (cells):* Represents the ratio of cells in which IPSCs were evoked in
464 response to optogenetic stimulation of Pkj cells (11/24, n=24 cells). *Right (trials):* Ratio of trials in which IPSCs were
465 successfully evoked. Each data point represents the mean from each cell (n=11 cells).

466 **E.** The average latency to the first action potential in a Pkj cell (n=9 cells) or first evoked IPSC in a UBC (n=11 cells).
467 Latency is calculated from the time of first pulse of 460 nm LED light. Each data point represents the mean (5-10
468 trials) from one cell.

469 **F.** Example data from one UBC shows a near complete inhibition of IPSCs (blue trace) after the application of 10 μM
470 gabazine (black trace).

471 **G.** Time course of reduction of IPSC amplitude by gabazine (n=9 cells).

472 **H.** Population data comparing peak IPSC amplitude before and after gabazine application (n=9 cells, paired t-test,
473 p=0.001).

474 **DISCUSSION**

475 In this study, we characterized the expression and function of Drd1 receptors in mGluR1+ (ON type) UBCs
476 of the cerebellar vermis. We leveraged the ability to genetically target these UBCs for electrophysiological
477 recording using the Drd1-Cre mouse line. We found changes in spontaneous activity of UBCs and their
478 NMDAR mediated currents by combining electrophysiological recordings with 2-photon glutamate uncaging
479 and 2-photon imaging. These effects are consistent with the literature on Drd1 receptor function across
480 multiple brain regions (Chen et al., 2004, 2007; Lahiri and Bevan, 2020). We evaluated several distinct
481 hypotheses for the source of dopamine to the cerebellum and found that neurons in the LC project to
482 cerebellar regions enriched in Drd1+ UBCs. Optogenetic activation of LC fibers elicited strong responses in
483 the dopaminergic optical sensor $GRAB_{DA2h}$ which is consistent with local DA co-release from TH+ LC
484 inputs. We found that UBCs receive direct inhibition from local Pkj cells, and that the activation of UBCs
485 can significantly alter the firing rate of Pkj cells, forming a closed reciprocal loop. These findings expand
486 our knowledge about neuromodulation in the cerebellum and reveal a new function for LC inputs in
487 cerebellar processing.

488 While the cerebellum is known to receive dense innervation from several neuromodulatory nuclei (Li et al.,
489 2014; Nelson et al., 1997; Schweighofer et al., 2004), questions about the role of these neuromodulators
490 have been difficult to address. The function of DA in the cerebellum has been particularly elusive due to
491 disagreement about the location of receptors and potential sources of DA (Hurley et al., 2003; Kim et al.,
492 2009; Locke et al., 2018; Mansour et al., 1991). To evaluate cerebellar DA receptor expression, we used a
493 combination of transgenic tools and FISH, characterizing the distribution of *Drd1a* mRNA in mGluR1a+
494 UBCs from the Drd1-EY262-Cre line crossed to a tdTomato reporter. Most Drd1 UBCs express a low
495 amount of *Drd1* transcripts. Since UBCs are compact cells with small somato-dendritic compartments, a
496 low transcript number of *Drd1a* mRNA could produce sufficient receptor levels to impact UBC activity.

497 We evaluated the consequences of Drd1 activation by recording the activity of Drd1+ UBCs before and
498 after activating Drd1 receptors. Most tdT+ UBCs (70%) increase their firing rate in response to Drd1
499 activation, as has been reported for Drd1 mediated effects on striatal spiny projection neurons (Lahiri and
500 Bevan, 2020). Quiescent neurons characterized by hyperpolarized resting membrane potential did not
501 initiate activity in response to pharmacological stimulus. This observation suggests several non-exclusive
502 possibilities. First, Drd1 receptor mediated depolarization may be insignificant in some UBCs. Second, the
503 effect of Drd1 agonism is, at least in part, dependent on ionic currents that are not active below a certain
504 membrane potential threshold. Third, the effect of Drd1 activation could be unable to overcome the ionic
505 currents that regulate the 'down' state in UBCs. One intriguing possibility is that previously described
506 bimodal states in UBC membrane potential (Diana et al., 2007) map onto distinct responses to
507 neuromodulatory inputs.

508 Based on previous literature on the mechanisms of dopamine neuromodulation in the mPFC (Chen et al.,
509 2004), we evaluated NMDAR-mediated currents in response to mossy fiber electrical stimulation, finding an
510 increase in NMDAR currents in the presence of a Drd1 agonist. We relied on two-photon glutamate
511 uncaging and imaging combined with electrophysiology to confirm the postsynaptic mechanism for Drd1-
512 dependent increase in NMDAR currents in UBCs. As compact neurons, UBCs have relatively small total
513 NMDA currents, yet this increase could have wide ranging consequences for cellular activity. The
514 enhancement in protein kinase A (PKA) activity, a consequence of Drd1 receptor activation, can promote
515 calcium flux through NMDARs (Skeberdis et al., 2006). Drd1 effects, mediated by $G\alpha_s$-coupled pathways,
516 have diverse impacts on neuronal channels in other cell types, raising the likelihood that currents in UBCs
517 are also altered by Drd1 activation. Of special note for Drd1+ UBCs, DA might enhance mGluR1 mediated
518 transient receptor potential channel (TRPC3) currents (Sekerková et al., 2013), as has been previously
519 demonstrated for striatal cholinergic interneurons (Chuhma et al., 2018). If so, this mechanism would have
520 synergistic effects with NMDA receptor-mediated current enhancements in response to Drd1 receptor
521 activation.

522 We next investigated three potential non-exclusive sources of DA to the cerebellum: the SNc/VTA, local
523 TH+ Pkj cells, and the LC. Consistent with some (Wagner et al., 2017), but not all previous reports
524 (Melchitzky, 2000; Panagopoulos et al., 1991), we found no evidence of projections from the SNc/VTA.
525 While we were able to confirm TH expression in nearby Pkj cells (Locke et al., 2020; Takada et al., 1993),
526 FISH analyses of *Ddc, Vmat2*, and *Dat* in the *Th*+ neurons confirm that these neurons lack the molecular
527 machinery for releasing DA. Previous work has found that while Pkj cells expressed TH, this protein is
528 maintained in an unphosphorylated state, unable to produce L-DOPA (Lee et al., 2006; Sawada et al.,
529 2004). Given the absence of L-DOPA synthesis, the function of TH in Pkj cells currently remains unknown.
530 However, there are other neuronal classes that express TH but lack complementary proteins for DA
531 release, including a subpopulation of olfactory bulb neurons (Chand et al., 2015), striatal GABAergic
532 interneurons (Weihe et al., 2006; Xenias et al., 2015), and cortical interneurons (Asmus et al., 2008). As
533 the final potential source of DA for UBCs, we evaluated the LC, known to project to the cerebellum (Bloom
534 et al., 1971; Schwarz et al., 2015) and verified here using retrograde AAV injections. Moreover, LC axons
535 have been previously shown to co-release DA and NE in other brain regions. DA released from LC fibers in
536 the hippocampus increases field excitatory postsynaptic currents (EPSCs) and contributes to memory
537 retention (Kempadoo et al., 2016; Takeuchi et al., 2016). In the paraventricular nucleus of the thalamus,
538 DA released by LC axons activates Drd2 receptors to decrease inhibitory input amplitude (Beas et al.,
539 2018). To test whether LC projections release DA onto UBCs, we used 2-photon imaging of genetically
540 encoded DA sensor $GRAB_{DA2h}$. Electrical or optogenetic activation of cerebellar LC axons increased
541 $GRAB_{DA2h}$ fluorescence in UBCs. Additional studies are needed to examine whether UBCs also express
542 multiple GPCRs that can be concurrently activated by LC inputs. Although $GRAB_{DA2h}$ is highly specific for
543 DA over NE (DA EC_{50}=0.13 μM, NE EC_{50}=1.7 μM) (Sun et al., 2020), we cannot exclude the possibility of
544 mixed monoamine release from LC axons with the results from optical dopamine sensors To address this

545 ambiguity we performed cell-attached recordings in UBCs, pharmacologically isolating Drd1 receptors, and
546 found an increase in firing rate after stimulation of LC fibers. To avoid effects of co-release of glutamate
547 from LC axons in these experiments, we had to block NMDAR, removing one downstream mechanism of
548 Drd1 activation in UBCs. In agreement with experiments examining Drd1 activation across different brain
549 regions, the persistence of Drd1 receptor mediated effects suggests that there are likely multiple
550 intracellular mechanisms governing UBC's response to dopamine.

551 The Drd1-Cre mouse line is one the few tools that allow us to selectively label subpopulations of UBCs.
552 Using ChR2, we took advantage of this mouse line to interrogate the potential function of UBCs within
553 vestibulo-cerebellar circuits. Despite the utility of acute slice preparation as a tool in electrophysiology, the
554 approach has important limitations, undercounting axonal inputs and impacting neural activity in
555 polysynaptic neuronal circuits. For this reason, we focused on Pkj cell firing rate changes on a short time
556 scale following optogenetic activation (500 ms), aiming to evaluate proximal effects downstream of
557 activating a small neuronal ensemble. The results from our experiments demonstrate that activation of
558 UBCs can induce pausing in a subset of local Pkj cells. Given our data examining Pkj cell E/I balance
559 during UBC optogenetic stimulation, changes in Pkj activity are likely explained by differential activation of
560 On and Off parallel fiber beams (Dizon and Khodakhah, 2011). 'On beam' parallel fibers, originating from
561 the granule cells directly below a Pkj neuron, make excitatory synapses onto that Pkj cell. Meanwhile,
562 granule cells that are not directly below a Pkj cell form 'Off beam' parallel fibers, activating molecular layer
563 interneurons and disynaptically inhibiting adjacent Pkj cells (Figure 5A). Both 'On' and 'Off' beam excitation
564 is likely to occur simultaneously; due to the spatial distribution of UBCs in the granular layer with whole-
565 field optogenetic activation protocol, 'Off beam' parallel fiber excitation is favored in the slice configuration.
566 How likely is it that similar concurrent activation of UBCs occurs *in vivo*? The majority of UBCs express
567 mGluR1 receptors and fire bursts of action potentials in response to glutamate release from mossy fibers
568 (Zampini et al., 2016). One possibility is that due to recurrent connections between UBCs, a burst of action
569 potentials in one UBC could cause a chain of activity leading to near simultaneous granular layer activity
570 across a large area. Future experiments are necessary to define the effects of UBCs activation *in vivo*, but
571 Pkj neuron recordings with optogenetic stimulation of UBCs can serve as a partial readout of the circuit
572 effects of neuromodulatory release of dopamine or other neuromodulators that enhance cerebellar UBC
573 activity.

574 In addition to functionally evaluating the evidence for Pkj-UBC connectivity to understand the placement of
575 Drd1+ UBCs within vestibulo-cerebellar circuits, our transsynaptic rabies virus tracing data confirmed the
576 labeling of Pkj cells, while also revealing the neuromodulatory inputs from the LC. Recent work has found
577 that Pkj cells in the vestibulo-cerebellum synapse onto nearby granule cells (Guo et al., 2016), but it
578 remained unknown whether local UBCs receive feedback input from Pkj cells. Notably, Pkj cell feedback to
579 granule cells appears to be restricted to the vestibular regions of the cerebellar cortex, with important
580 implications for the recurrent activity of Pkj cells in these lobules. Our findings expand the recurrent

581 vestibulo-cerebellar circuit to include UBCs. Since UBCs diverge in the granular layer, any circuit level
582 effects from feedback inhibition via Pkj cells is likely to be amplified. These inhibitory connections have also
583 been described in parallel work by another lab (Canton-Josh et al., 2021; Guo et al., 2021a, 2021b) for
584 mGluR1+ UBCs. There is longstanding evidence of the LC modulating Pkj cell activity through the release
585 of norepinephrine (Basile and Dunwiddie, 1984; Lippiello et al., 2015) and recent work shows adrenergic
586 signaling in Golgi cells as well (Lanore et al., 2019). Our findings suggest that the LC could release
587 dopamine onto other cells in the cerebellum, such as Drd2 expressing Pkj cells (Kim et al., 2009; Mengod
588 et al., 1989), in addition to UBCs. Although no past research has focused on adrenergic receptor
589 expression in UBCs, it is possible that LC axons could mediate their effect on UBCs through
590 norepinephrine, in addition to dopamine.

591 Unipolar brush cells have been found in three distinct brain circuits implicated in the cancelation of self-
592 generated cues due to an animal's movement (Requarth and Sawtell, 2014; Singla et al., 2017; Warren
593 and Sawtell, 2016). Their position in the input layer of the cerebellum means that their activity can
594 significantly alter mossy fiber signals to the cerebellum. In the mouse cerebellum, Drd1 expressing UBCs
595 reside in regions involved in processing vestibular signals and eye movements. Since we find that Drd1
596 receptors are expressed predominantly in ON UBCs, DA release from LC axons could coordinate with
597 vestibular mossy fiber inputs to enhance signals arising directly from the semicircular canals (Balmer and
598 Trussell, 2019). Leveraging genetic access to a subpopulation of UBCs we have characterized a new
599 recurrent subcircuit between Pkj cells and UBCs, which has the potential to significantly regulate the output
600 of the vestibulo-cerebellum. Altogether, this work expands our knowledge of cerebellar circuitry, resolves
601 longstanding questions about the ability of TH+ Pkj cells to release DA, and points to the LC as the source
602 of DA to the cerebellum.

603 **DATA AVAILABILITY**

604 All data and code generated or analyzed during this study are included in the manuscript and supporting
605 files.

606 **AUTHOR CONTRIBUTIONS**

607 J.E.C and Y.K. conceived the experiments. Anatomical, IHC, and FISH experiments were performed and
608 analyzed by J.E.C., J.Q, and J.S. Electrophysiology and two-photon imaging experiments were performed
609 and analyzed by J.E.C. J.E.C. and Y.K. wrote the manuscript, with input from other authors.

610 **ACKNOWLEDGMENTS**

611 This work was supported by the Rita Allen Foundation Scholar Award, NINDS R01NS107539, Searle
612 Scholar Award, the Beckman Young Investigator Award, William and Bernice E. Bumpus Young Innovator
613 Award, NARSAD Young Investigator and P&S Fund Grant (all Y.K.). J.E.C. was supported as a trainee on
614 an NIH/NINDS institutional training grant (T32NS041234) and with a Ruth Kirschstein National Research
615 Service Award (NRSA) Individual Predoctoral Fellowship (NINDS 1F31NS120736). We thank Dr. Tiffany
616 Schmidt and Northwestern University Biological Imaging Facility for the use of their confocal microscopes,
617 and Lindsey Butler for mouse colony management. We are grateful to Dr. Bernardo Sabatini for the gift of
618 retrograde AAV virus, Dr. Horwitz for the gift of Pcp2 promoter ChR2 AAV, Dr. Yulong Li for sharing the
619 $GRAB_{DA2h}$ virus, and Dr. Raj Awatramani for the TH-Flpo mouse line. We thank Dr. Michael Priest and
620 Samuel Minkowicz for feedback on this manuscript.

621

622 **METHODS**

623 **Materials and Methods**

624 **Mouse Lines**

625 All experiments were performed under the guidelines set by Northwestern University Institutional Animal
626 Care and Use Committee (IACUC). All mice used were on the C57BL/6 background (P20-80). Mice of both
627 sexes were used; sex was tracked for every experiment, and data were analyzed for any differences.
628 Several transgenic lines were used for this project, acquired from Jackson laboratory (Bell Harbor, MA). To
629 visualize Drd1a-positive cells expression we used a heterozygous mouse line with insertion of Cre
630 recombinase at the Drd1a locus (Drd1a-Cre, GENSAT, founder line EY262) (Gong S. Zheng C., 2003). In
631 order to label cells expressing dopamine transporter (DAT) we used knock-in mice expressing Cre
632 recombinase under DAT promoter, B6.SJL-Slc6a3 $^{tm1.1(cre)Bkmn}$/J mice (*DAT* $^{i\text{-}Cre}$)(Jackson Lab, # 006660)
633 (Bäckman et al., 2006). To label tyrosine hydroxylase positive neurons we used a TH-Flpo developed by
634 the lab of Dr. Raj Awatramani (Poulin et al., 2018). Depending on experiments these Cre lines were either
635 injected with a viral vector or crossed with a floxed tdTomato reporter mouse line (Ai14, Jackson Lab,
636 #007914) (Madisen et al., 2010).

637

638 **Viral vectors**

639 Viruses were acquired from Addgene, UNC vector core, Columbia vector core, Salk Institute, and WZ
640 Biosciences. For stimulation of Drd1-Cre+ UBCs we injected AAV5-EF1a-DIO-hChR2(H134R)-eYFP-
641 WPRE-hGH (7.2x1012 vg/ml, Addgene, 20298P). For experiments with optogenetic stimulation of Pkj cells
642 we injected AAV1-PCP2-CHR2-mCherry ($7.2x10^{12}$ vg/ml) (El-Shamayleh et al., 2017) and AAV8-Flex-GFP
643 (6.2 x1012 vg/ml, UNC vector core). For pseudo-typed rabies tracing experiments, the viruses were AAV1-
644 CAG-Flex-H2B-eGFP-N2c(G) (2.5×10^{12} gc/ml, Columbia Vector Core), AAV1-EF1α-FLEX-GT (4.3×10^{11}
645 gc/ml, Salk Institute viral vector core), and CVS-N2cΔG tdTomato EnvA (Columbia vector core). For

646 retrograde labelling of TH fibers to the cerebellum, we used AAV2/retro-CAG-fDIO-Cre-EGFP (a gift from
647 the laboratory of Bernardo Sabatini). For anterograde labeling of LC fibers, we injected AAV1-CAG-
648 FLEXFRT-ChR2(H134R)-mCherry (75470, $7x10^{12}$ vg/mL, Addgene). For imaging DA dynamics, we used
649 AAV9-hSyn-DIO-DA4.3, ($GRAB_{DA2h}$, 20191018, $2.7x10^{13}$ vg/mL, WZ Biosciences; plasmid, gift from the
650 laboratory of Yulong Li).
651
652 **Surgical procedures**
653 Animals were anesthetized using an isoflurane vaporizer, with oxygen flow rate maintained at 1.00
654 liter/minute. Induction was done with 2-3% isoflurane and maintenance at 1.5-2%. Tail pinches were used
655 to ensure the effectiveness of anesthesia. Animal was mounted on a stereotaxic frame (David Kopf
656 Instruments, Tujunga, CA), ear bars were inserted, and a chemical depilator as used to expose the skin.
657 Skin was cleaned with iodine followed by alcohol, using aseptic technique. Injections of AAV viral vectors
658 or CTB-488 (Thermo Fisher, C34775) were made using a pulled glass pipette and a UltraMicroPump
659 controller (World Precision Instruments, Sarasota, FL) at a rate of 100 nl/minute. Rabies virus injected were
660 performed in a BSL2 hood. Cerebellar stereotaxic coordinates: AP: -2.5 mm ML: 0 mm, from lambda, DV: -
661 2.5 mm from surface of brain. Coordinates for the locus coeruleus: AP: -0.9 mm ML: 0.9 mm, from lambda,
662 DV: -3.2 mm from surface of brain. All animals received an I.P. injection of ketoprofen (0.1 mg/20 g) 0
663 hours, 24 hours and 48 hours after surgery, with approved post-surgical monitoring. Mice recovered 1
664 week for retrograde CTB-488 injections and 2-6 weeks for viral vector injections. For modified rabies virus
665 tracing experiments, we allowed the helper viruses to express for 4-6 weeks before injecting rabies virus.
666
667 **Immunohistochemistry**
668 Animals were anesthetized using isoflurane and then transcardially perfused with 4% paraformaldehyde.
669 The brain was extracted and post-fixed at 4ºC in 4% PFA overnight, transferred to phosphate buffered
670 saline (PBS) and stored a 4 ºC. The brain was mounted onto a Leica VT1000s vibratome and 50 µm thick
671 sections were made. Sections were stored in well plates in PBS at 4 ºC. Slices were permeabilized in 0.2%
672 Triton-X, then blocked in 10% BSA with 0.05% Triton-X and incubated in primary antibody for 24-48 hours
673 at 4ºC in 0.2% Triton-X. the tissue underwent 3 10-minute rinse steps in PBS and was then incubated in a
674 secondary antibody for 2 hours at RT. Primary antibodies: Rabbit anti-Calretinin (1:500, Swant, CR7697),
675 Mouse anti-mGluR1a (1:500, BD Biosciences, G209-2048), Sheep anti-TH (1:1000, Abcam, ab113),
676 Chicken anti-Tbr2 (1:1000, Sigma-Aldrich, AB15894). Secondary antibodies: Goat Anti-Mouse 647 (1:1000,
677 Life Technologies, A-21236), Goat Anti-Rabbit 488(1:1000, Life Technologies A-11034), Donkey-anti-
678 Sheep 647 (1:1000, Thermo Fisher Scientific, A-21448), Goat anti-Chicken IgY (H+L) secondary antibody,
679 Alexa Fluor 488 (1:1000, Life Technologies A-11039). IHC samples were mounted onto Superfrost Plus
680 slides (ThermoFisher Scientific, Waltham, MA) dried and cover slipped under glycerol:TBS (3:1) with
681 Hoechst 33342 (1:1000; ThermoFisher Scientific). Slides were imaged at 10X magnification on a slide
682 scanning microscope Olympus VS120 slide scanning microscope (Olympus, Waltham, MA). For IHC

683 quantification slides were imaged using a Leica SP5 confocal microscope (Leica Microsystems) with a
684 40/63X objective. Z stacks at 2-5 µm step sizes were acquired and images were analyzed in ImageJ (FIJI)
685 (Schindelin et al., 2012).
686
687 **Fluorescence in situ hybridization**
688 Following anesthetization using isoflurane, the mouse was decapitated, and the brain was quickly removed,
689 placed into OCT and frozen on dry ice. Sample was placed in -80ºC freezer for at least 1 night. Tissue was
690 sliced on a cryostat (Leica CM1850) at a thickness of 20 µm and mounted onto Superfrost Plus slides
691 (ThermoFisher Scientific, Waltham, MA). Slices were placed in a slide box and in a Freezer safe Ziploc bag
692 and placed in a -80 ºC freezer overnight before processing. Samples were fixed with 4% PFA in 0.1 M PBS
693 at 4˚C, processed according to RNAscope Fluorescent Multiplex Assay manual for fresh frozen tissue
694 (Advanced Cell Diagnostics, Newark, CA) and coverslipped using ProLong Gold antifade reagent with
695 DAPI (Molecular Probes). Several probes were used including: *tdT (*ACDBio Cat No. 317041*), Drd1a*
696 *(*ACDBio, Cat No. 406491-C2*), Th (*ACDBio, Cat No. 317621-C2*), Vmat2 (Slc18a2,* ACDBio Cat No.
697 425331-C3*), Ddc (*ACDBio, Cat No. 318681*), Dat (Slc6a3*, ACDBio, Cat No. 315441). Slides were imaged
698 on a Leica SP5 confocal in two channels using a 63x objective digital zoom 1.5x with 0.5-micron z steps
699 (512 x 512 pixels). FISH images were analyzed using ImageJ (Schindelin et al., 2012). Images were
700 background subtracted and thresholded. We then used 3D objects counter (Bolte and Cordelieres, 2006) to
701 create a 3-dimensional object. The 3D ROI manager (Ollion et al., 2013) plugin was used to create regions
702 of interest. The tdT channel was used to as a label for UBC soma and to establish ROI. Once ROIs was
703 acquired, we quantified the overlap of signals by counting the number of *Drd1a* puncta within each cell.
704
705 **Acute slice preparation**
706 Mice (P20-60) were deeply anesthetized with isoflurane, followed by a transcardial perfusion using 34ºC
707 (Huang and Uusisaari, 2013) ACSF (artificial cerebrospinal fluid) containing (mM) 127 NaCl, 2.5 KCl, 1.25
708 NaH_2PO_4, 25 $NaHCO_3$, 20 glucose, 2 $CaCl_2$, and 1 $MgCl_2$. After perfusion mice were decapitated, brain
709 was removed, blocked, mounted, and placed into a chamber containing 34ºC ACSF oxygenated with 95%
710 O_2, 5% CO_2. Parasagittal 300 µm cerebellar brain slices were made using a vibratome (Leica VT1200s).
711 Slices were transferred to a holding chamber containing 34ºC ACSF oxygenated with 95% O_2, 5% CO_2,
712 and were incubated for 30 minutes before being cooled to room temperature (22-24ºC).
713
714 **Electrophysiology**
715 All recordings were performed on an acute slice electrophysiology system (Scientifica, UK); neurons were
716 visualized using a 60X water-immersion objective (Olympus, Tokyo, Japan) imaged using a QIClick
717 microscope camera (QImaging, Surrey, Canada), under DIC. Slices were placed in the recording chamber
718 and perfused with oxygenated ACSF at a rate of 2 ml/min, with temperature as noted. For UBC recordings,
719 cells expressing tdTomato in a Drd1-Cre; tdT cross were targeted using epifluorescence illumination from a

720 CoolLED pe4000 system (CoolLED Ltd., Andover, UK). Whole-cell patch electrodes were pulled from
721 borosilicate capillary glass to have a resistance of 2.5-5 MΩ for UBC recordings and 1-2 MΩ for Pkj
722 recordings. All recordings were digitized at 10-20 kHz and filtered at 3-4 kHz using a Multiclamp 700b
723 amplifier (Axon Instruments, Union City, CA), acquired using a version of the MATLAB-based (MathWorks,
724 Natick, MA) acquisition suite, ScanImage (Pologruto et al., 2003).
725
726 **Current clamp recordings**
727 UBCs were targeted using a Drd1-Cre;Tdt transgenic mouse line (P20-40). Slices were perfused with
728 ACSF at RT (22-24 ºC). For current clamp recording any cells with a series resistance >40 MΩ or an action
729 potential peak below 10 mV were excluded from analysis. Intracellular solution used was (in mM) 135 K-
730 gluconate, 4 KCl,10 HEPES, 10 Na-phosphocreatine, 4 MgATP, 0.4 Na_2GTP, 1 EGTA, 20 µM Alexa 488
731 (pH 7.2-7.3, 295-298 mOsm/L). A measured liquid junction potential of ~12 mV was corrected for post-hoc
732 before analysis. Every sweep was 15 seconds long, with a 20 second ITI between each trial. Within each
733 trial, a 500 ms hyperpolarizing step 10-20 pA was injected in order to measure input resistance. In cells
734 that did not have spontaneous firing we injected a 500 ms long depolarizing pulse to assess cell health and
735 ability to fire action potentials. Both the period of hyperpolarizing pulse and the depolarizing pulse were
736 excluded from analysis of spontaneous firing rate. We analyzed spontaneous activity, passive membrane
737 properties, and action potential shape. After break-in we waited ~13 minutes period before acquiring
738 baseline firing properties of the UBCs. The baseline period lasted ~7 min (20 trials) before we applied
739 SKF81297. To activate Drd1 receptors we puff applied SKF81297 (500 µM) using a 300 ms long
740 PicoSpritzer puff (Parker Hannifin, Hollis, NH). The drug was applied once per trial (20 s ITI) for a 10-
741 minute period (30 trials). We continued recording after drug application for a 10-minute (30 trials) washout
742 period. The glass puff pipette was pulled to have a ~5 µm opening. The puff pipette was placed 20-40 µm
743 above tissue surface and 50-75 µm away from cell on the x-axis. Care was taken to ensure there was no
744 movement of the slice due to the puff. After the recording, each UBC was imaged to verify that it was filled
745 with Alexa dye, and then a 10X magnification image was taken to record location within the cerebellum.
746
747 **Voltage clamp recordings**
748 UBCs were targeted using a Drd1-Cre;tdT transgenic mouse line (P20-40). Voltage clamp recordings were
749 performed in ACSF (32-34ºC). Cells were excluded if they had a series resistance >25 MΩ or if series
750 resistance changed >20% during the recording. We did not use series resistance compensation. The
751 internal electrode solution contained (in mM): 125 $CsMeSO_3$, 5 HEPES-Cs, 0.4 EGTA, 10
752 Phosphocreatine disodium salt, 2 ATP-Mg, 0.5 GTP-Mg, 5 TEA-Cl, 2 QX314-Cl, 20 µM Alexa 488 (pH 7.2-
753 7.3, 295-298 mOsm/L). We corrected for liquid junction potential (~8 mV) before acquiring data. In order to
754 isolate NMDAR currents, 1 µM Gabazine (Tocris, 1262), 1 µM NBQX (Tocris, 0373), 1 µM strychnine
755 (Sigma-Aldrich, S8753) were added to the ACSF bath. Cells were held at +40 mV and we used 0 mM MgCl
756 to minimize the Mg block of NMDA receptors. A tungsten bipolar electrode (CBAPB75, FHC Inc) was

757 lowered into nearby white matter at least 100 µm away from UBC being recorded. Each electrical
758 stimulation consisted of 5 pulses, 200 Hz, 100-150 µA, 50-80 µs pulse width. Each trial was 7 seconds long,
759 with an intertrial interval of 30 seconds. Every trial included a 500 ms long 20 mV hyperpolarizing pulse to
760 measure series resistance. We acquired current traces during a baseline period of 20 minutes (40 trials),
761 followed by a flow-in of SKF81297 (10µM) for 15 minutes (30 trials) before washing out the drug.
762
763 **Optogenetic stimulation of Drd1-Cre UBCs**
764 Pkj cells within 100 µm of ChR2-EYFP expressing UBCs were targeted for recording. Recordings were
765 performed in ACSF (32-34 ºC). We recorded baseline firing rate of Purkinje cells in cell-attached mode,
766 loose seal (50-200 M Ohms). To stimulate ChR2 in UBCs we used trains of light pulses (1 ms, 10-20 Hz,
767 20 pulses, 460 nM, 2-5 mW) delivered through a 60X water-immersion objective (Olympus, Tokyo, Japan)
768 with CoolLED PE4000 widefield illumination (CoolLED Ltd., Andover, UK). Every trial was 15 seconds long,
769 with an ITI of 20 seconds. After a ~7 min (20 trials) baseline period, we stimulated ChR2 for 30 trials.
770 Afterwards a 10-minute (30 trials) recording with no stimulation was acquired. For each slice, we verified
771 that we could reliably evoke action potentials in nearby EYFP+ UBC with this stimulation protocol.
772
773 For the experiments with EPSC and IPSC recordings, we used an internal solution consisting of 125
774 $CsMeSO_3$, 5 HEPES-Cs, 0.4 EGTA, 10 Phosphocreatine disodium salt, 2 ATP-Mg, 0.5 GTP-Mg, 5 TEA-Cl,
775 2 QX314-Cl, 20 µM Alexa 488 (pH 7.2-7.3, 295-298 mOsm/L). We corrected for liquid junction potential (~8
776 mV). We first achieved a Giga-Ohm seal on the Pkj cell before recording cell-attached action potentials, to
777 evaluate the response of Pkj cells to UBC optogenetic activation before breaking into the Pkj cell and
778 recording synaptic currents. We recorded EPSCs while holding the cell at -70 mV (5 trials), then slowly
779 increasing the holding voltage to 0 mV and recording IPSCs (5 trials).
780
781 **IPSC recordings in UBCs**
782 Drd1-Cre animals were injected with AAV1-PCP2-ChR2-mCherry and AAV8-Flex-GFP. Acutely prepared
783 brain slices were perfused with ACSF at RT (22-24ºC) to slow down spontaneous firing rate of Pkj cells.
784 We used epifluorescence to verify expression of mCherry in nearby Pkj cells, with very brief GFP
785 illumination to target UBCs for patch clamping without stimulating ChR2. We used an internal solution with
786 a high concentration of Cl^- ions (in mM): 150 CsCl, 4 NaCl, 0.5 $CaCl_2$, 10 HEPES-Cs, 5 EGTA-Cs, 10
787 Phosphocreatine disodium salt, 2 ATP-Mg, 0.5 GTP-Na, 2 QX314-Br, 20 µM Alexa 488 (pH 7.2-7.3, 295-
788 298 mOsm/L). We corrected for liquid junction potential (~3 mV). Starting 5 minutes after break-in, we
789 recorded 10 trials/UBC, where every trial was 15 seconds long, with an ITI of 60 seconds. During every
790 trial, we delivered an optogenetic stimulus train (1 ms, 100 Hz, 100 pulses, 460 nM, 2-5 mW) through a
791 60X water-immersion objective (Olympus, Tokyo, Japan) with CoolLED illumination PE4000. For a subset
792 of experiments, after 5 trials we added 10 µM Gabazine to the bath. For every slice, cell-attached
793 recordings were used to verify efficient optogenetic stimulation of Pkj cell firing.

794 **Cell attached recordings**

795 UBCs were targeted using a Drd1-Cre;tdTomato transgenic mouse line (P20-40). Cell-attached recordings
796 were performed in ACSF (32-34ºC). Internal electrode solution contained (in mM): 125 $CsMeSO_3$, 5
797 HEPES-Cs, 0.4 EGTA, 10 Phosphocreatine disodium salt, 2 ATP-Mg, 0.5 GTP-Mg, 5 TEA-Cl, 2 QX314-Cl,
798 20 µM Alexa 488 (pH 7.2-7.3, 295-298 mOsm/L). Every sweep was 15 seconds long, ITI 20 seconds. After
799 a ~16 min (50 trials) baseline period we flowed in 10 µM SKF81297 (Tocris 1447) into the bath. Cells
800 showing spontaneous firing were included in analysis for continual monitoring of cell health. For
801 experiments using LC optogenetic stimulation we included the following in the bath: Prazosin (10 µM),
802 propranolol (10 µM), NBQX (5 µM), CPP (10 µM), Pyr-3 (1 µM), gabazine (10 µM) and strychnine (1 µM).
803 For recording in the presence of Drd1 antagonist, 5 µM SCH39166 was present in the bath. During every
804 trial, we delivered an optogenetic stimulus train (1 ms, 20 Hz, 50 pulses, 460 nM, 2-5 mW) through a 60X
805 water-immersion objective (Olympus, Tokyo, Japan) with CoolLED illumination PE300, with a 20 second
806 inter-trial interval.

807

808 **Two-photon imaging and glutamate uncaging experiments**

809 Slices were perfused with ACSF at RT (22-24ºC). Experiments were done on a modified acute slice
810 electrophysiology Scientifica microscope using a 60X water immersion objective**.** Two mode-locked
811 Ti:Sapphire lasers (Mai Tai eHP and Mai Tai eHP DS, Newport) were used for two-photon fluorescence
812 imaging and for uncaging, with the wavelengths of 910 nm and 725 nm, respectively (Banala et al., 2018;
813 Chen et al., 2020; Kozorovitskiy et al., 2015; Wu et al., 2021; Xiao et al., 2018). The location of the laser
814 beam was controlled by a two-dimensional galvanometer scanning mirror system (HSA Galvo 8315K,
815 Cambridge Technology). Fluorescence emission was passed through a dichroic beamsplitter (FF670-
816 SDi01-26x38, Semrock) and a bandpass filter (FF02-520/28, Semrock). Emission light was collected by
817 two PMTs (H10770P, Hamamatsu). MATLAB script-based data acquisition software ScanImage (Pologruto
818 et al., 2003) was used to acquire images. Laser intensity was controlled by Pockels cells, with laser power
819 at the sample plane of 10-15 mW. For glutamate uncaging experiments, to isolate NMDAR currents the
820 following drugs were included in the ACSF bath: 1 µM TTX (Tocris, 1069), 1 µM Gabazine (Tocris, 1262), 1
821 µM NBQX (Tocris, 0373), 1 µM strychnine (Sigma-Aldrich, S8753), 1 µM Pyr-3 (Tocris,3753), 1 mM MNI-
822 caged-L-glutamate. Images were acquired at 2X magnification, sampled at 15.6 Hz continuously, 1 ms
823 dwell time per pixel, 256 x 256. Uncaging was performed using 1 ms pulses at 725 nm power (10-20 mW).
824 Each trial was 15 seconds long with a 60 second ITI between trials. The mean NMDAR current for each
825 cell was calculated across all trials that evoked a response.

826

827 For two-photon experiments imaging $GRAB_{DA2h}$ data were acquired with a 3.9 Hz sampling rate, each trial
828 lasted ~25 seconds with an ITI of 150 seconds. A monopolar stimulating electrode was placed 100-200 µm
829 away from cell being imaged within white matter tracts. The electrical stimulation (50 pulses, 50 Hz, 100 µs
830 pulse width, 100-300 µA) was delivered every 150 seconds. Five to ten baseline trials were acquired before

831 the flow-in of Drd2 antagonist (1 μM L-741,626). For optogenetic experiments, the same imaging
832 parameters as for electrical stimulation experiments were used. Instead of electrical stimulation, CoolLED
833 pe300 (CoolLED Ltd., Andover, UK) was used to activate ChR2 (200 pulses at 39 Hz, 2 ms pulses, 460 nm,
834 3-5 mW/cm^2). For these experiments we visually verified the expression of ChR2+ in LC axons post hoc,
835 using the fused mCherry fluorophore. To avoid activating TH+ Pkj cells, we excluded acute slices from
836 animals with Pkj cells expressing mCherry.
837
838 **Pharmacology**
839 All drugs were purchased from Sigma Aldrich (St. Louis, MO), or Tocris (Bristol, UK). SKF 81297
840 hydrobromide (Tocris, 1447) was applied either as puff (500 μM) or flow in (10 μM) depending on
841 experiment type. All other drugs were bath applied: SCH-39166 hydrobromide (Tocris,2299), SCH-23390
842 hydrochloride (Tocris, 0925), SKF-83566 hydrobromide (Tocris, 1586), Strychnine (Sigma-Aldrich, 8753),
843 Tetraethylammonium chloride (Sigma-Aldrich, 86614), TTX (Tocris Bioscience, 1069), (RS)-CPP (Tocris
844 Bioscience, 0173), NBQX (Tocris Bioscience, 0373), SR 95531 hydrobromide (Tocris Bioscience, 1262),
845 MNI-caged-L-glutamate (Tocris Biosciences 1490), L-741,626 (Tocris Bioscience, 1003), Pyr-3
846 (Tocris,3753), prazosin (Sigma-Aldrich, P7791), propranolol (Sigma-Aldrich, 40543), quinpirole
847 hydrochloride (Tocris Bioscience, 1061). For experiments requiring pharmacological agents dissolved in
848 DMSO the total bath concentration never exceeded 0.02% DMSO.
849
850 **Analysis and statistics**
851 No statistical methods were used to pre-determine sample sizes, but our sample sizes are similar to those
852 reported in previous publications using similar methods. Custom MATLAB (MathWorks, Natick, MA) scripts
853 were used for analysis of electrophysiology data. For current clamp recordings we analyzed membrane
854 voltage, firing rate, input resistance, and action potential half width. Membrane voltage was calculated
855 using a median filter to exclude changes due to action potential firing. Data from cell-attached recordings
856 were used to quantify spontaneous firing rate without perturbing the membrane. Data from voltage clamp
857 recordings were first baseline subtracted and then analyzed for width, peak of evoked current traces and
858 total charge of evoked currents. For all electrophysiological recordings reported mean values from each
859 cell are the average of 10 trials. Fluorescence intensity signals from $GRAAB_{DA2h}$ imaging experiments were
860 measured in FIJI (Schindelin et al., 2012), data were then analyzed in MATLAB. Fluorescence signal for
861 each trial was normalized as ΔF/F. Summary values were aggregated in GraphPad Prism 5 (GraphPad,
862 LaJolla, CA) for all statistical tests. All population data were tested for normality using Shapiro-Wilk
863 normality test, D'Agostino & Pearson omnibus normality test, and KS normality test. Paired t-test or paired
864 Mann-Whitney U test were used, as appropriate. For comparisons between current clamp datasets, we
865 used Kruskal-Wallis test with Dunn's multiple comparison post hoc tests. In all figures, bars represent
866 mean +/- SEM. To compare EPSC/IPSC ratios and changes in Pkj cell firing rates we used a simple linear
867 regression. Group allocation was randomized, as indicated in our methods section under the analysis and

868 statistics subsection. All data analysis used batch processing with the same code and parameters. For
869 histological analyses comparing expression of proteins or mRNA between brain regions the same intensity
870 and size thresholds were applied.
871

872 **REFERENCES**

873 Abbott, L.C., Isaacs, K.R., and Heckroth, J.A. (1996). Co-localization of tyrosine hydroxylase and Zebrin II
874 immunoreactivities in Purkinje cells of the mutant mice, tottering and tottering/leaner. Neuroscience *71*,
875 461–475.

876 Altman, J., and Bayer, S.A. (1977). Time of origin and distribution of a new cell type in the rat cerebellar
877 cortex. Exp. Brain Res. *29*, 265–274.

878 Aosaki, T., Kiuchi, K., and Kawaguchi, Y. (1998). Dopamine D1-like receptor activation excites rat striatal
879 large aspiny neurons in vitro. J. Neurosci. *18*, 5180–5190.

880 Asmus, S.E., Anderson, E.K., Ball, M.W., Barnes, B.A., Bohnen, A.M., Brown, A.M., Hartley, L.J., Lally,
881 M.C., Lundblad, T.M., Martin, J.B., et al. (2008). Neurochemical characterization of tyrosine hydroxylase-
882 immunoreactive interneurons in the developing rat cerebral cortex. Brain Res. *1222*, 95–105.

883 Austin, M.C., Schultzberg, M., Abbott, L.C., Montpied, P., Evers, J.R., Paul, S.M., and Crawley, J.N.
884 (1992). Expression of tyrosine hydroxylase in cerebellar Purkinje neurons of the mutant tottering and leaner
885 mouse. Mol. Brain Res. *15*, 227–240.

886 Bäckman, C., Malik, N., Zhang, Y., Shan, L., Grinberg, A., Hoffer, B., Westphal, H., and Tomac, A. (2006).
887 Characterization of a mouse strain expressing Cre recombinase from the 3' untranslated region of the
888 dopamine transporter locus. Genesis *44*, 383–390.

889 Balmer, T.S., and Trussell, L.O. (2019). Selective targeting of unipolar brush cell subtypes by cerebellar
890 mossy fibers. Elife *8*, 1–28.

891 Banala, S., Arvin, M.C., Bannon, N.M., Jin, X.T., Macklin, J.J., Wang, Y., Peng, C., Zhao, G., Marshall, J.J.,
892 Gee, K.R., et al. (2018). Photoactivatable drugs for nicotinic optopharmacology. Nat. Methods *15*, 347–
893 350.

894 Basile, A.S., and Dunwiddie, T. V. (1984). Norepinephrine elicits both excitatory and responses from
895 Purkinje cells in the in vitro rat cerebellar slice. Brain Res. *296*, 15–25.

896 Beas, B.S., Wright, B.J., Skirzewski, M., Leng, Y., Hyun, J.H., Koita, O., Ringelberg, N., Kwon, H.-B.,
897 Buonanno, A., and Penzo, M.A. (2018). The locus coeruleus drives disinhibition in the midline thalamus via
898 a dopaminergic mechanism. Nat. Neurosci. *21*, 963–973.

899 Bloom, F.E., Hoffer, B.J., and Siggins, G.R. (1971). Studies on norepinephrine-containing afferents to
900 Purkinje cells of rat cerebellum. I. Localization of the fibers and their synapses. Brain Res. *25*, 501–521.

901 Bolte, S., and Cordelieres, F.P. (2006). A guided tour into subcellular colocalisation analysis in light
902 microscopy. J. Microsc. *224*, 13–232.

903 Borges-Merjane, C., and Trussell, L.O. (2015). ON and OFF unipolar brush cells transform multisensory
904 inputs to the auditory system. Neuron *85*, 1029–1042.

905 Canton-Josh, J.E., Qin, J., and Kozorovitskiy, Y. (2021). Dopaminergic regulation of vestibulo-cerebellar
906 circuits through unipolar brush cells. BioRxiv 437266.

907 Carey, M.R., and Regehr, W.G. (2009). Noradrenergic Control of Associative Synaptic Plasticity by
908 Selective Modulation of Instructive Signals. Neuron *62*, 112–122.

909 Cerminara, N.L., Lang, E.J., Sillitoe, R. V., and Apps, R. (2015). Redefining the cerebellar cortex as an
910 assembly of non-uniform Purkinje cell microcircuits. Nat. Rev. Neurosci. *16*, 79–93.

911 Chand, A.N., Galliano, E., Chesters, R.A., and Grubb, M.S. (2015). A distinct subtype of dopaminergic
912 interneuron displays inverted structural plasticity at the axon initial segment. J. Neurosci. *35*, 1573–1590.

913 Chen, C., Soto, G., Dumrongprechachan, V., Bannon, N., Kang, S., Kozorovitskiy, Y., and Parisiadou, L.
914 (2020). Pathway-specific dysregulation of striatal excitatory synapses by LRRK2 mutations. Elife *9*, 1–26.

915 Chen, G., Greengard, P., and Yan, Z. (2004). Potentiation of NMDA receptor currents by dopamine D1
916 receptors in prefrontal cortex. Proc. Natl. Acad. Sci. U. S. A. *101*, 2596–2600.

917 Chen, L., Bohanick, J.D., Nishihara, M., Seamans, J.K., and Yang, C.R. (2007). Dopamine D1/5 receptor-
918 mediated long-term potentiation of intrinsic excitability in rat prefrontal cortical neurons: Ca2+-dependent
919 intracellular signaling. J. Neurophysiol. *97*, 2448–2464.

920 Chuhma, N., Mingote, S., Yetnikoff, L., Kalmbach, A., Ma, T., Ztaou, S., Sienna, A.-C., Tepler, S., Poulin,
921 J.-F., Ansorge, M., et al. (2018). Dopamine neuron glutamate cotransmission evokes a delayed excitation
922 in lateral dorsal striatal cholinergic interneurons. Elife *7*, 1–29.

923 Chung, S.-H., Marzban, H., Watanabe, M., and Hawkes, R. (2009). Phospholipase Cbeta4 expression
924 identifies a novel subset of unipolar brush cells in the adult mouse cerebellum. Cerebellum *8*, 267–276.

925 Chung, S.-H., Kim, C.-T., Jeong, Y.-G., and Lee, N.-S. (2010). TBR2-immunopsitive unipolar brush cells
926 are associated with ectopic zebrin II-immunoreactive Purkinje cell clusters in the cerebellum of scrambler
927 mice. Anat. Cell Biol. *43*, 72.

928 Cutando, L., Puighermanal, E., Castell, L., Tarot, P., Belle, M., Bertaso, F., Arango-Lievano, M., Ango, F.,

929 Rubinstein, M., Chédotal, A., et al. (2019). Cerebellar dopamine D2 receptors regulate preference for social
930 novelty. BioRxiv 884288.

931 Diana, M.A., Otsu, Y., Maton, G., Collin, T., Chat, M., and Dieudonne, S. (2007). T-Type and L-Type Ca2+
932 Conductances Define and Encode the Bimodal Firing Pattern of Vestibulocerebellar Unipolar Brush Cells.
933 J. Neurosci. *27*, 3823–3838.

934 Dizon, M.J., and Khodakhah, K. (2011). The role of interneurons in shaping Purkinje cell responses in the
935 cerebellar cortex. J. Neurosci. *31*, 10463–10473.

936 El-Shamayleh, Y., Kojima, Y., Soetedjo, R., and Horwitz, G.D. (2017). Selective Optogenetic Control of
937 Purkinje Cells in Monkey Cerebellum. Neuron *95*, 51–62.

938 Englund, C. (2006). Unipolar Brush Cells of the Cerebellum Are Produced in the Rhombic Lip and Migrate
939 through Developing White Matter. J. Neurosci. *26*, 9184–9195.

940 Fung, S.J., Reddy, V.K., Liu, R.H., Wang, Z., and Barnes, C.D. (1994). Existence of glutamate in
941 noradrenergic locus coeruleus neurons of rodents. Brain Res. Bull. *35*, 505–512.

942 Giovannucci, A., Badura, A., Deverett, B., Najafi, F., Pereira, T.D., Gao, Z., Ozden, I., Kloth, A.D.,
943 Pnevmatikakis, E., Paninski, L., et al. (2017). Cerebellar granule cells acquire a widespread predictive
944 feedback signal during motor learning. Nat. Neurosci. *20*, 727–734.

945 Gong S. Zheng C., D.M.L. et al (2003). A gene expression atlas of the central nervous system based on
946 artificial chromosomes. Nature *425*, 917–925.

947 Gorelova, N.A., and Yang, C.R. (2000). Dopamine D1/D5 Receptor Activation Modulates a Persistent
948 Sodium Current in Rat Prefrontal Cortical Neurons In Vitro. J. Neurophysiol. *84*, 75–87.

949 Guo, C., Witter, L., Rudolph, S., Elliott, H.L., Ennis, K.A., and Regehr, W.G. (2016). Purkinje Cells Directly
950 Inhibit Granule Cells in Specialized Regions of the Cerebellar Cortex. Neuron *91*, 1330–1341.

951 Guo, C., Rudolph, S., Neuwirth, M.E., and Regehr, W.G. (2021a). Purkinje cell outputs selectively inhibit a
952 subset of unipolar brush cells in the input layer of the cerebellar cortex. Elife *10*, 1–17.

953 Guo, C., Rudolph, S., Neuwirth, M.E., and Regehr, W.G. (2021b). Purkinje cell outputs selectively inhibit a
954 subset of unipolar brush cells in the input layer of the cerebellar cortex. BioRxiv 437031.

955 Hernandez-Lopez, S., Bargas, J., Surmeier, D.J., Reyes, A., and Galarraga, E. (1997). D1 receptor
956 activation enhances evoked discharge in neostriatal medium spiny neurons by modulating an L-type Ca2+
957 conductance. J Neurosci *17*, 3334–3342.

958 Houck, B.D., and Person, A.L. (2015). Cerebellar premotor output neurons collateralize to innervate the

959 cerebellar cortex. J. Comp. Neurol. *523*, 2254–2271.

960 Huang, S., and Uusisaari, M.Y. (2013). Physiological temperature during brain slicing enhances the quality
961 of acute slice preparations. Front. Cell. Neurosci. *7*, 48.

962 Huang, Y., Zhang, Q., Song, N.-N., Zhang, L., Sun, Y.-L., Hu, L., Chen, J.-Y., Zhu, W., Li, J., and Ding, Y.-
963 Q. (2016). Lrp5/6 are required for cerebellar development and for suppressing TH expression in Purkinje
964 cells via β-catenin. Mol. Brain *9*, 7.

965 Hurley, M.J., Mash, D.C., and Jenner, P. (2003). Markers for dopaminergic neurotransmission in the
966 cerebellum in normal individuals and patients with Parkinson's disease examined by RT-PCR. Eur. J.
967 Neurosci. *18*, 2668–2672.

968 Judd, E.N., Lewis, S.M., and Person, A.L. (2021). Diverse inhibitory projections from the cerebellar
969 interposed nucleus. Elife *10*, 1–28.

970 Kalmbach, B.E., Davis, T., Ohyama, T., Riusech, F., Nores, W.L., and Mauk, M.D. (2010). Cerebellar
971 cortex contributions to the expression and timing of conditioned eyelid responses. J. Neurophysiol. *103*,
972 2039–2049.

973 Kawahara, H., Kawahara, Y., and Westerink, B.H.C. (2001). The noradrenaline-dopamine interaction in the
974 rat medial prefrontal cortex studied by multi-probe microdialysis. Eur. J. Pharmacol. *418*, 177–186.

975 Kempadoo, K.A., Mosharov, E. V., Choi, S.J., Sulzer, D., and Kandel, E.R. (2016). Dopamine release from
976 the locus coeruleus to the dorsal hippocampus promotes spatial learning and memory. Proc. Natl. Acad.
977 Sci. *113*, 14835–14840.

978 Kim, J.A., Sekerková, G., Mugnaini, E., and Martina, M. (2012). Electrophysiological, morphological, and
979 topological properties of two histochemically distinct subpopulations of cerebellar unipolar brush cells.
980 Cerebellum *11*, 1012–1021.

981 Kim, Y.S., Shin, J.H., Hall, F.S., and Linden, D.J. (2009). Dopamine signaling is required for depolarization-
982 induced slow current in cerebellar Purkinje cells. J. Neurosci. *29*, 8530–8538.

983 Kozorovitskiy, Y., Peixoto, R., Wang, W., Saunders, A., and Sabatini, B.L. (2015). Neuromodulation of
984 excitatory synaptogenesis in striatal development. Elife *4*, 1–18.

985 Lahiri, A.K., and Bevan, M.D. (2020). Dopaminergic Transmission Rapidly and Persistently Enhances
986 Excitability of D1 Receptor-Expressing Striatal Projection Neurons. Neuron *106*, 277-290.e6.

987 Lanore, F., Rothman, J.S., Coyle, D., and Silver, R.A. (2019). Norepinephrine controls the gain of the
988 inhibitory circuit in the cerebellar input layer. BioRxiv 567172.

989 Lee, N.S., Kim, C.T., Han, S.Y., Kawk, J.H., Sawada, K., Fukui, Y., and Jeong, Y.G. (2006). The absence
990 of phosphorylated tyrosine hydroxylase expression in the Purkinje cells of the ataxic mutant pogo mouse.
991 J. Vet. Med. Ser. C Anat. Histol. Embryol. *35*, 178–183.

992 Li, B., Zhu, J., and Wang, J. (2014). Histaminergic afferent system in the cerebellum : structure and
993 function. Cerebellum & Ataxias *1*, 1–9.

994 Lippiello, P., Hoxha, E., Volpicelli, F., Lo Duca, G., Tempia, F., and Miniaci, M.C. (2015). Noradrenergic
995 modulation of the parallel fiber-Purkinje cell synapse in mouse cerebellum. Neuropharmacology *89*, 33–42.

996 Locke, T.M., Soden, M.E., Miller, S.M., Hunker, A., Knakal, C., Licholai, J.A., Dhillon, K.S., Keene, C.D.,
997 Zweifel, L.S., and Carlson, E.S. (2018). Dopamine D1 Receptor–Positive Neurons in the Lateral Nucleus of
998 the Cerebellum Contribute to Cognitive Behavior. Biol. Psychiatry *84*, 401–412.

999 Locke, T.M., Fujita, H., Hunker, A., Johanson, S.S., Darvas, M., du Lac, S., Zweifel, L.S., and Carlson, E.S.
1000 (2020). Purkinje Cell-Specific Knockout of Tyrosine Hydroxylase Impairs Cognitive Behaviors. Front. Cell.
1001 Neurosci. *14*, 1–16.

1002 Madisen, L., Zwingman, T.A., Sunkin, S.M., Oh, S.W., Zariwala, H.A., Gu, H., Ng, L.L., Palmiter, R.D.,
1003 Hawrylycz, M.J., Jones, A.R., et al. (2010). A robust and high-throughput Cre reporting and
1004 characterization system for the whole mouse brain. Nat. Neurosci. *13*, 133–140.

1005 Mansour, A., Meador-Woodruff, J.H., Zhou, Q.Y., Civelli, O., Akil, H., and Watson, S.J. (1991). A
1006 comparison of D1 receptor binding and mRNA in rat brain using receptor autoradiographic and in situ
1007 hybridization techniques. Neuroscience *45*, 359–371.

1008 Melchitzky, D. (2000). Tyrosine Hydroxylase- and Dopamine Transporter-Immunoreactive Axons in the
1009 Primate Cerebellum Evidence for a Lobular- and Laminar-Specific Dopamine Innervation.
1010 Neuropsychopharmacology *22*, 466–472.

1011 Mengod, G., Inocencia Martinez-Mir, M., Teresa Vilaro, M., and Palacios, J.M. (1989). Localization of the
1012 mRNA for the dopamine D2 receptor in the rat brain by in situ hybridization histochemistry. Neurobiology
1013 *86*, 8560–8564.

1014 Mugnaini, E., and Floris, A. (1994). The unipolar brush cell: A neglected neuron of the mammalian
1015 cerebellar cortex. J. Comp. Neurol. *339*, 174–180.

1016 Nelson, T.E., King, J.S., and Bishop, G.A. (1997). Distribution of tyrosine hydroxylase-immunoreactive
1017 afferents to the cerebellum differs between species. J. Comp. Neurol. *379*, 443–454.

1018 Ollion, J., Cochennec, J., Loll, F., Escudé, C., and Boudier, T. (2013). TANGO: A generic tool for high-
1019 throughput 3D image analysis for studying nuclear organization. Bioinformatics *29*, 1840–1841.

1020 Panagopoulos, N.T., Papadopoulos, G.C., and Matsokis, N. a. (1991). Dopaminergic innervation and
1021 binding in the rat cerebellum. Neurosci. Lett. *130*, 208–212.

1022 Panagopoulos, N.T., Matsokis, N. a, and Valcana, T. (1993). Cerebellar and striatal dopamine receptors:
1023 effects of reeler and weaver murine mutations. J. Neurosci. Res. *35*, 499–506.

1024 Patriarchi, T., Cho, J.R., Merten, K., Howe, M.W., Marley, A., Xiong, W., Folk, R.W., Broussard, G.J.,
1025 Liang, R., Jang, M.J., et al. (2018). Ultrafast neuronal imaging of dopamine dynamics with designed
1026 genetically encoded sensors. Science. *360*, 1–15.

1027 Pologruto, T.A., Sabatini, B.L., and Svoboda, K. (2003). ScanImage: Flexible software for operating laser
1028 scanning microscopes. Biomed. Eng. Online *2*, 1–9.

1029 Poulin, J.F., Caronia, G., Hofer, C., Cui, Q., Helm, B., Ramakrishnan, C., Chan, C.S., Dombeck, D.A.,
1030 Deisseroth, K., and Awatramani, R. (2018). Mapping projections of molecularly defined dopamine neuron
1031 subtypes using intersectional genetic approaches. Nat. Neurosci. *21*, 1260–1271.

1032 Rajakumar, N., Hrycyshyn, A.W., and Flumerfelt, B.A. (1992). Afferent organization of the lateral reticular
1033 nucleus in the rat: An anterograde tracing study. Anat. Embryol. (Berl). *185*, 25–37.

1034 Raymond, J.L., and Lisberger, S.G. (1998). Neural Learning Rules for the Vestibulo-Ocular Reflex. J.
1035 Neurosci. *18*, 9112–9129.

1036 Reardon, T.R., Murray, A.J., Turi, G.F., Wirblich, C., Croce, K.R., Schnell, M.J., Jessell, T.M., and
1037 Losonczy, A. (2016). Rabies Virus CVS-N2cδG Strain Enhances Retrograde Synaptic Transfer and
1038 Neuronal Viability. Neuron *89*, 711–724.

1039 Requarth, T., and Sawtell, N.B. (2014). Plastic Corollary Discharge Predicts Sensory Consequences of
1040 Movements in a Cerebellum-Like Circuit. Neuron *82*, 896–907.

1041 Rogers, A., and Beier, K.T. (2021). Can transsynaptic viral strategies be used to reveal functional aspects
1042 of neural circuitry? J. Neurosci. Methods *348*, 109005.

1043 Sabatini, B.L., and Tian, L. (2020). Imaging Neurotransmitter and Neuromodulator Dynamics In Vivo with
1044 Genetically Encoded Indicators. Neuron *108*, 17–32.

1045 Sakai, M., Fujii, T., Karasawa, N., Arai, R., and Nagatsu, I. (1995). Enhanced expression of tyrosine
1046 hydroxylase and aromatic l-amino acid decarboxylase in cerebellar Purkinje cells of mouse after
1047 hyperosmotic stimuli. Neurosci. Lett. *194*, 142–144.

1048 Sawada, K., Ando, M., Sakata-Haga, H., Sun, X., Jeong, Y., Hisano, S., Takeda, N., and Fukui, Y. (2004).
1049 Abnormal expression of tyrosine hydroxylase not accompanied by phosphorylation at serine 40 in
1050 cerebellar Purkinje cells of ataxic mutant mice, rolling mouse Nagoya and dilute-lethal. Congenit. Anom.

1051 (Kyoto). *44*, 46–50.

1052 Schindelin, J., Arganda-Carreras, I., Frise, E., Kaynig, V., Longair, M., Pietzsch, T., Preibisch, S., Rueden,
1053 C., Saalfeld, S., Schmid, B., et al. (2012). Fiji: An open-source platform for biological-image analysis. Nat.
1054 Methods *9*, 676–682.

1055 Schneider, C.A., Rasband, W.S., and Eliceiri, K.W. (2012). NIH Image to ImageJ: 25 years of image
1056 analysis. Nat. Methods *9*, 671–675.

1057 Schwarz, L.A., Miyamichi, K., Gao, X.J., Beier, K.T., Weissbourd, B., DeLoach, K.E., Ren, J., Ibanes, S.,
1058 Malenka, R.C., Kremer, E.J., et al. (2015). Viral-genetic tracing of the input–output organization of a central
1059 noradrenaline circuit. Nature *524*, 88–92.

1060 Schweighofer, N., Doya, K., and Kuroda, S. (2004). Cerebellar aminergic neuromodulation: towards a
1061 functional understanding. Brain Res. Brain Res. Rev. *44*, 103–116.

1062 Sekerková, G., Kim, J.-A., Nigro, M.J., Becker, E.B.E., Hartmann, J., Birnbaumer, L., Mugnaini, E., and
1063 Martina, M. (2013). Early onset of ataxia in moonwalker mice is accompanied by complete ablation of type
1064 II unipolar brush cells and Purkinje cell dysfunction. J. Neurosci. *33*, 19689–19694.

1065 Singla, S., Dempsey, C., Warren, R., Enikolopov, A.G., and Sawtell, N.B. (2017). A cerebellum-like circuit
1066 in the auditory system cancels responses to self-generated sounds. Nat. Neurosci. *20*, 943–950.

1067 Skeberdis, V.A., Chevaleyre, V., Lau, C.G., Goldberg, J.H., Pettit, D.L., Suadicani, S.O., Lin, Y., Bennett,
1068 M.V.L., Yuste, R., Castillo, P.E., et al. (2006). Protein kinase A regulates calcium permeability of NMDA
1069 receptors. Nat. Neurosci. *9*, 501–510.

1070 Stoof, J.C., and Kebabian, J.W. (1984). Two dopamine receptors: Biochemistry, physiology and
1071 pharmacology. Life Sci. *35*, 2281–2296.

1072 Sun, F., Zeng, J., Jing, M., Zhou, J., Feng, J., Owen, S.F., Luo, Y., Li, F., Wang, H., Yamaguchi, T., et al.
1073 (2018). A Genetically Encoded Fluorescent Sensor Enables Rapid and Specific Detection of Dopamine in
1074 Flies, Fish, and Mice. Cell *174*, 481-496.e19.

1075 Sun, F., Zhou, J., Dai, B., Qian, T., Zeng, J., Li, X., Zhuo, Y., Zhang, Y., Wang, Y., Qian, C., et al. (2020).
1076 Next-generation GRAB sensors for monitoring dopaminergic activity in vivo. Nat. Methods *17*, 1156–1166.

1077 Surmeier, D.J., and Kitai, S.T. (1993). D1 and D2 dopamine receptor modulation of sodium and potassium
1078 currents in rat neostriatal neurons. Prog. Brain Res. *99*, 309–324.

1079 Takada, M., Sugimoto, T., and Hattori, T. (1993). Tyrosine hydroxylase immunoreactivity in cerebellar
1080 Purkinje cells of the rat. Neurosci. Lett. *150*, 61–64.

1081 Takeuchi, T., Duszkiewicz, A.J., Sonneborn, A., Spooner, P.A., Yamasaki, M., Watanabe, M., Smith, C.C.,
1082 Fernández, G., Deisseroth, K., Greene, R.W., et al. (2016). Locus coeruleus and dopaminergic
1083 consolidation of everyday memory. Nature *537*, 357–362.

1084 Wagner, M.J., Kim, T.H., Savall, J., Schnitzer, M.J., and Luo, L. (2017). Cerebellar granule cells encode
1085 the expectation of reward. Nature *544*, 96–100.

1086 Wall, N.R., DeLaParra, M., Callaway, E.M., and Kreitzer, A.C. (2013). Differential innervation of direct- and
1087 indirect-pathway striatal projection neurons. Neuron *79*, 347–360.

1088 Warren, R., and Sawtell, N.B. (2016). A comparative approach to cerebellar function: insights from
1089 electrosensory systems. Curr. Opin. Neurobiol. *41*, 31–37.

1090 Watanabe, D., and Nakanishi, S. (2003). mGluR2 postsynaptically senses granule cell inputs at golgi cell
1091 synapses. Neuron *39*, 821–829.

1092 Weihe, E., Depboylu, C., Schütz, B., Schäfer, M.K.H., and Eiden, L.E. (2006). Three types of tyrosine
1093 hydroxylase-positive CNS neurons distinguished by dopa decarboxylase and VMAT2 co-expression. Cell.
1094 Mol. Neurobiol. *26*, 659–678.

1095 Woodruff-pak, D.S. (1993). Eyeblink Classical Conditioning in H . M .: Delay and Trace Paradigms. Behav.
1096 Neurosci. *107*, 911–925.

1097 Wu, H.S., Sugihara, I., and Shinoda, Y. (1999). Projection patterns of single mossy fibers originating from
1098 the lateral reticular nucleus in the rat cerebellar cortex and nuclei. J. Comp. Neurol. *411*, 97–118.

1099 Wu, M., Minkowicz, S., Dumrongprechachan, V., Hamilton, P., and Kozorovitskiy, Y. (2021). Ketamine
1100 Rapidly Enhances Glutamate-Evoked Dendritic Spinogenesis in Medial Prefrontal Cortex Through
1101 Dopaminergic Mechanisms. Biol. Psychiatry *89*, 1096–1105.

1102 Xenias, H.S., Ibanez-Sandoval, O., Koos, T., and Tepper, J.M. (2015). Are Striatal Tyrosine Hydroxylase
1103 Interneurons Dopaminergic? J. Neurosci. *35*, 6584–6599.

1104 Xiao, L., Priest, M.F., and Kozorovitskiy, Y. (2018). Oxytocin functions as a spatiotemporal filter for
1105 excitatory synaptic inputs to VTA dopamine neurons. Elife *7*, 1–26.

1106 Yang, B., Sanches-Padilla, J., Kondapalli, J., Morison, S.L., Delpire, E., Awatramani, R., and Surmeier,
1107 D.J. (2021). Locus coeruleus anchors a trisynaptic circuit controlling fear-induced suppression of feeding.
1108 Neuron *109*, 823-838.e6.

1109 Zampini, V., Liu, J.K., Diana, M.A., Maldonado, P.P., Brunel, N., and Dieudonné, S. (2016). Mechanisms
1110 and functional roles of glutamatergic synapse diversity in a cerebellar circuit. Elife *5*, 1–25.

Supplementary Information

Dopaminergic regulation of vestibulo-cerebellar circuits through unipolar brush cells

Jose Ernesto Canton-Josh, Joanna Qin, Joseph Salvo, Yevgenia Kozorovitskiy*

Department of Neurobiology, Northwestern University, Evanston, IL 60208

*Corresponding author: Yevgenia.Kozorovitskiy@northwestern.edu

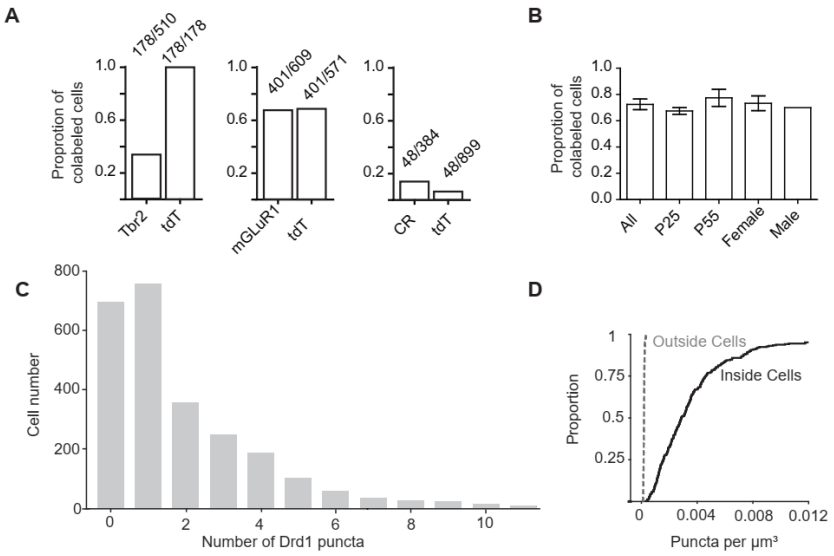

Figure 1—figure supplement 1. Co-localization of tdT+ UBCs with UBC subtype markers and Drd1 mRNA.

A. The proportion of cells co-labeled by known immunohistochemical markers of UBC subtypes and tdT in Drd1-Cre; tdT mouse line. *Left*: A subset of Tbr2+ UBCs were co-labeled by tdTomato, while all tdT+ cells expressed Tbr2 protein. *Center*: tdT+ and mGluR1+ UBCs show substantial overlap. *Right:* Few CR+ UBCs express tdT. Ratios represent the population of co-labeled cells divided by the total number of cells expressing a given marker.

B. A comparison of *Drd1*+ tdTomato+ UBCs between two age groups and across sex show similar proportions of UBCs that express *Drd1* transcripts. (n=4 total mice, P25 n=2, P55 n=2, Female n=3, Male n=1).

C. A histogram of the number of *Drd1* puncta per each UBC tdT+ soma (n=4 mice, 2553 cells).

D. 3D quantification of *Drd1* puncta per unit volume shows 40-fold enrichment within the somata of UBCs expressing tdT, compared to regions outside tdT+ ROIs.

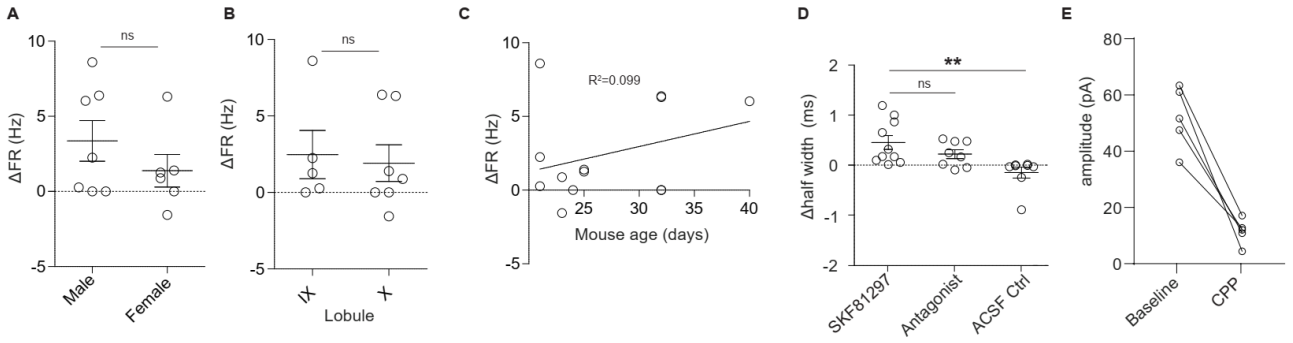

Figure 2—figure supplement 1. Characterization of Drd1 receptor activation effects on UBC firing and postsynaptic currents.

A. Comparison of changes in firing rate in response to SKF81297 application shows no difference across sex (unpaired t-test, Mann-Whitney U test, p=0.42).

B. Comparison of changes in firing rate in response to SKF81297 application across lobules IX and X of the vermis (unpaired t-test, Mann-Whitney U test, p=0.62).

C. Comparison of changes in firing rate in response to SKF81297 application across age (P20-P40) (R^2=0.099, ns).

D. Comparison of changes in action potential half-width shows an increase with application of SKF81297, but not ACSF (Kruskal-Wallis test, p=0.0026, Dunn's multiple comparison test, *p<0.05, ** p<0.01).

E. NMDAR currents modulated by Drd1 activation are largely blocked by flow in of 10 μM CPP.

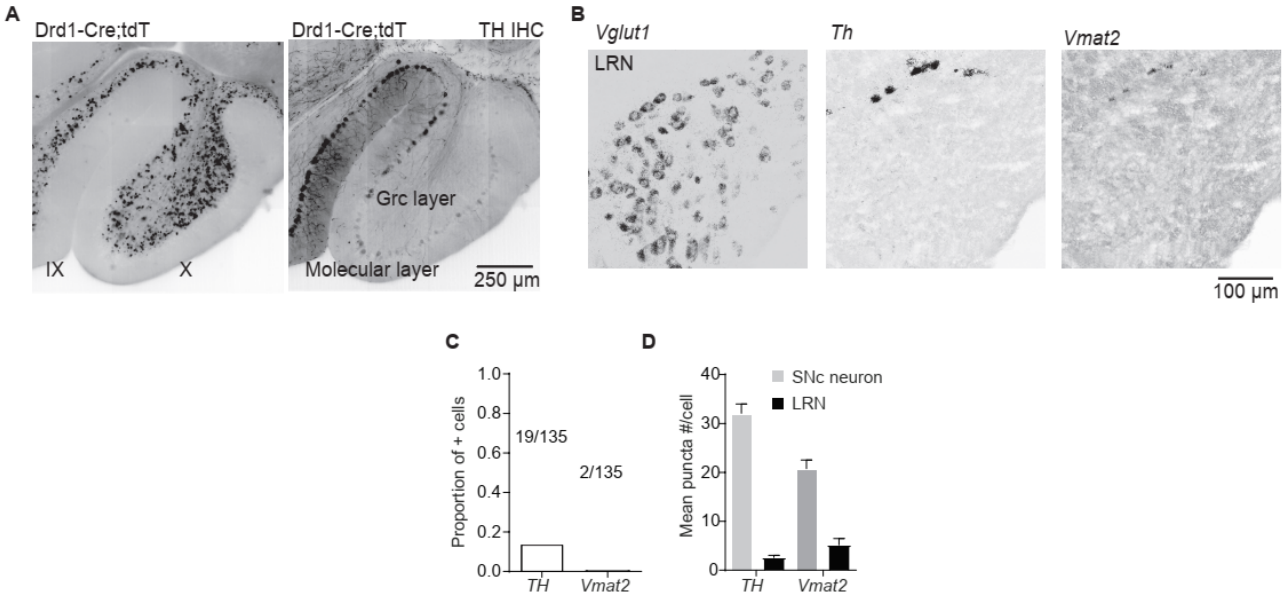

Figure 3—figure supplement 1. Potential dopamine sources for vestibulo-cerebellum.

A. Example images from the cerebellum of Drd1a-Cre;tdT mouse, immunolabelled for TH, showing TH+ Pkj cells and tdT+ UBCs in lobules IX/X of the cerebellar vermis. Scale bar, 250 µm.

B. LRN neurons, labeled by *Vglut1* show little overlap with *Th* or vesicular monoamine transporter type 2 *(Vmat2)* Scale bar, 100 µm.

C. Quantification of transcripts involved in synthesis and release of DA. *Top*: Few LRN neurons express transcripts for *Vmat2* or *Th*.

D. The few LRN neurons (n=3 mice) that express *Vmat2* and *Th* express low transcript numbers in comparison to SNc neurons (n=2 mice). Grey bars represent counts from SNc DA neurons, black bars represent LRN cells.

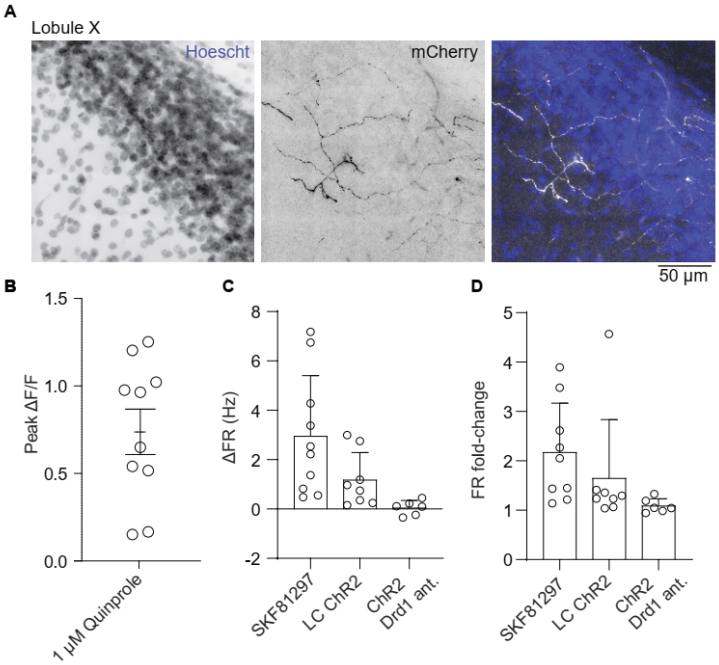

Figure 5—figure supplement 1. Structural and functional evaluation of DA release from LC fibers in the cerebellum.

A. Images of LC axons in the granular and molecular layer of lobule X after injection of AAV1-CAG-FLEXFRT-ChR2(H134R)-mCherry into the LC. Greyscale LUT for left and middle panels; for overlay image, inverted greyscale (mCherry) and blue (Hoescht). Scale bar, 50 µm.

B. Peak fluorescence change in $GRAB_{DA}$ expressing UBCs after a flow-in of Drd2 agonist (1 µM quinpirole).

C. Comparison of changes in firing rate in response to SKF81297, optogenetic activation of LC fibers, and optogenetic LC activation in the presence of Drd1 antagonist.

D. Same as C but for firing rate fold changes.

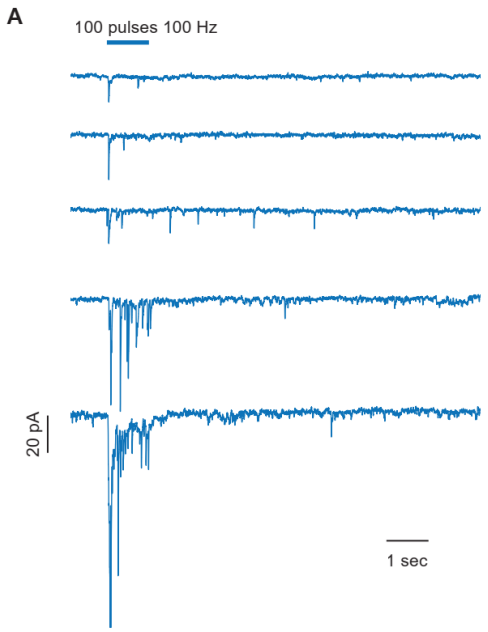

Figure 7—figure supplement 1. Inhibitory postsynaptic currents in UBCs in response to Pkj optogenetic activation.

A. Single trial example traces from 5 different UBCs show variability in the amplitude of response across cells, on the background of low spontaneous IPSC rate, after optogenetic stimulation of Pkj cells. Scale bar, 20 pA, 1 sec.